# Energetics of Boreal Wintertime Blocking Highs around the Ural Mountains

Ning SHI[1*], Yicheng WANG[2], and Suolangtajie[3]

1 *Collaborative Innovation Center on Forecast and Evaluation of Meteorological Disasters, Key Laboratory of Meteorological Disaster, Ministry of Education, Nanjing University of Information Science & Technology, Nanjing* 210044

2 *College of Atmospheric Science, Nanjing University of Information Science & Technology, Nanjing* 210044

3 *Tibet Institute of Plateau Atmospheric and Environmental Sciences, Tibet Meteorological Bureau, Lhasa* 850000

(Received April 15, 2021; in final form September 28, 2021)

ABSTRACT

Based on the daily Japanese 55-yr reanalysis data, this study analyzes the maintenance mechanism for 53 boreal winter blocking highs around the Ural Mountains (UBHs) during 1958–2018 based on the atmospheric energy budget equations. After decomposing the circulation into background flow, low-frequency anomalies, and high-frequency eddies, it was found that the interaction between the background flow and low-frequency anomalies is conducive to the maintenance of the UBHs. Due to the southwestward gradient in the climatological mean air temperature over the Eurasian continent, it is easy for the air temperature anomalies as well as the wind velocity anomalies in the middle and lower troposphere induced by the UBHs to facilitate the positive conversion of baroclinic energy associated with the background flow into the UBHs. Likewise, the conversion of barotropic energy associated with the background flow is also evident in the upper troposphere, in which the climatological mean westerlies have evident southward gradient to the northwest of Lake Baikal and southwestward gradient over Barents Sea. Note that the conversion of baroclinic energy associated with the background flow is dominant throughout the lifecycle of UBHs, acting as the major contributor to the maintenance of the UBHs. Although transient eddies facilitate maintenance of the UBHs via positive conversion of barotropic energy in the middle and upper troposphere, they hinder the maintenance of UBHs via negative conversion of baroclinic energy in the lower troposphere. The diabatic heating anomalies tend to counteract the local air temperature anomalies in the middle and lower troposphere, which damps the available potential energy of UBHs and acts as a negative contributor to the UBHs.

**Key words:** blocking highs around the Ural Mountains, energy budget, background flow, transient eddies

**Citation:** Shi, N., Y. C. Wang, and Suolangtajie, 2022: Energetics of boreal wintertime blocking highs around the Ural Mountains. *J. Meteor. Res.*, **36**(1), 154–174, doi: 10.1007/s13351-022-1069-7.

## 1. Introduction

Blocking high is a planetary-scale circulation phenomenon over the middle and high latitudes. Due to its longevity and stationarity, a blocking high usually induces persistent abnormal weather situations. However, due to the complexity of blocking high, its formation and maintenance mechanisms pose a challenge to the medium-range weather forecasts (Matsueda and Palmer, 2018) and future projections (Woollings et al., 2018). It has been a primary interest of many synoptic and dynamical meteorologists for decades.

In the Northern Hemisphere, winter blocking highs preferentially occur over Euro-Atlantic region and central and eastern Pacific (e.g., Dole and Gordon, 1983; Tibaldi and Molteni, 1990; Pelly and Hoskins, 2003; Schwierz et al., 2004; Barriopedro et al., 2006), which are the climatological areas of planetary ridge and the exit zones of two main storm tracks (Barriopedro et al., 2010). The formation of the blocking highs over the two regions is associated with the interaction between the planetary-scale circulation and the migratory transient eddies (Green, 1977; Illari and Marshall, 1983; Colucci, 1985; Holopainen and Fortelius, 1987; Nakamura et al., 1997). Transient eddies can systematically transport anticyclonic vorticity into blocking highs (Shutts, 1983; Mullen, 1987), induce positive height tendency (Holo-

Supported by the National Natural Science Foundation of China (42088101, 42025502, 41575057, and 41975063) and Qing Lan Project of Jiangsu Province, China.

*Corresponding author: shining@nuist.edu.cn

painen and Fortelius, 1987; Nakamura et al., 1997), and transfer their kinetic energy (KE) and/or available potential energy (APE) to the planetary-scale or time-mean circulation which is associated with blocking highs (Hansen and Chen, 1982; Hansen and Sutera, 1984; Holopainen and Fortelius, 1987; Lu and Huang, 1996; Ma and Liang, 2017). In addition to the diagnostic analyses, the theoretical models also verified the important role of the interaction for transient eddies with the planetary waves and mean flow in forming the main features of blocking flow (Luo, 2000, 2005; Luo et al., 2014, 2019).

Ural Mountains are usually considered as the third most preferential region for the occurrence of blocking highs over the Northern Hemisphere in winter (Dole and Gordon, 1983; Lupo and Smith, 1995). Blocking highs around the Ural Mountains (UBHs for simplicity) are regarded as an important upstream precursor of severe cold surges in East Asia (Tao, 1957; Takaya and Nakamura, 2005; Wen et al., 2009; Zhou et al., 2009; Bueh et al., 2011a, b; Luo et al., 2016a, b). Previous studies have revealed that the low-frequency dynamics, e.g., Rossby wave propagation over the Eurasian continent, is evident for the formation of the UBHs (Luo et al., 2016b; Shi et al., 2020), which is also true for Europe blocking highs in boreal winter (Nakamura, 1994; Nakamura et al., 1997) and the blocking highs around the Far East in boreal summer (Nakamura and Fukamachi, 2004; Shi et al., 2016). The Rossby wave propagation is emanated from the North Atlantic (Li, 2004) or a decaying positive North Atlantic Oscillation event (Luo et al., 2007, 2015). As for the high-frequency dynamics, the feedback forcing of high-frequency eddies does not exert significant influence on the mid- and upper troposphere during the evolution of UBHs (Li, 2004; Luo et al., 2016b; Shi et al., 2020), which differentiates UBHs from the oceanic blocking highs.

Note that, for the dynamical features of UBHs in the sub-seasonal timescales, Shi et al. (2020) discussed the high-frequency and low-frequency dynamics separately in different dynamical contexts. Specifically, the contribution from high-frequency migratory eddies is evaluated through the potential tendency equation (Lau and Holopainen, 1984), while the contribution from low-frequency dynamics, i.e., the Rossby wave propagation, is represented by the wave-activity flux which is derived from the enstrophy tendency equation and the energy tendency equation (Takaya and Nakamura, 2001). Thus, it is difficult to evaluate the relative contributions of low-frequency dynamics and high-frequency dynamics to the maintenance of UBHs. Cheung et al. (2013) explored the dynamical features of UBHs via the geostrophic vorticity tendency equation, and the thermodynamic features via the thermodynamic equations. They found that the horizontal advections of both air temperature and absolute vorticity are the important contributors to the maintenance of UBHs. Likewise, Li et al. (2020) found that the convergence/divergence of the stationary momentum and heat fluxes are prior to the evolution of UBHs, indicating the importance of both dynamical and thermodynamical processes in modulating the evolution of UBHs. However, the relative importance of dynamical and thermodynamical processes is not obvious since different equations (Cheung et al., 2013) or only indices are used (Li et al., 2020). Recently, with the budget equation of local finite-amplitude wave activity (Huang and Nakamura, 2016), Nakamura and Huang (2018) emphasized the important role of the convergence of zonal wave activity flux in initiating the blocking. Wang et al. (2021) further pinpointed that the eddy heat flux assists zonal wave activity flux in UBHs initiation and stagnation. Although barotropic and baroclinic processes, wave propagation and advection are well discussed by Wang et al. (2021) in the evolution of UBHs, it is still not clear what important role high-frequency eddies play, which is generally emphasized by previous studies on blocking. Therefore, it is meaningful to take into consideration all the physical processes in one uniform context to deepen our knowledge on the dynamics of UBHs. As elucidated in Tanaka et al. (2016) on the dynamics of the western Pacific atmospheric teleconnection pattern, the diagnostic equation of energy is a suitable diagnostic tool for exploring the relative importance of the dynamical and thermodynamical processes, and/or the high-frequency dynamics and the low-frequency dynamics. Inspired by their study, the present study also utilizes the diagnostic equation of energy to discuss the underlying mechanism for the maintenance of UBHs.

Simmons et al. (1983) demonstrated that the product of the barotropic component of the extended Eliassen–Palm flux ($\overline{v'^2 - u'^2}, -\overline{u'v'}$) (Hoskins et al., 1983) and the horizontal gradient of the background velocity fields corresponds to the barotropic energy conversion between the background circulation and the disturbance. In addition, Kosaka and Nakamura (2006) demonstrated that the product of baroclinic component of the extended Eliassen–Palm flux ($fv'b'/N^2$) and the horizontal gradient of the background air temperature field corresponds to the baroclinic energy conversion. Therefore, the interference with the background flow can facilitate the formation and maintenance of low-frequency circulation anomalies. In fact, some studies have pinpointed that low-frequency circulation anomalies can maintain themselves

through the effective conversion of the barotropic energy and/or baroclinic energy associated with the background circulation (Simmons et al., 1983; Nakamura et al., 1987; Kosaka and Nakamura, 2006, 2010; Cai et al., 2007; Kosaka et al., 2009; Jiang et al., 2013; Tanaka et al., 2016; Dai et al., 2021). These low-frequency anomalies are generally close to or along the jet stream, indicating the important role of the jet stream in forming the low frequency anomalies. For example, the wintertime Pacific/North American pattern and East Atlantic pattern are located to the exit of jet stream, and they can effectively extract the barotropic energy from the background flow (Simmons et al., 1983; Nakamura et al., 1987); the summertime Silk Road pattern, which is along the subtropical jet stream over the Eurasian continent, can effectively extract the baroclinic energy from the background flow (Kosaka et al., 2009). In addition, the conversion of both barotropic and baroclinic energy associated with background flow is also evident during the evolution of the blocking highs over the North Atlantic (Ma and Liang, 2017) that are close to the Atlantic jet stream. Unlike the aforementioned low-frequency circulation anomalies, UBHs are located in the region with relatively weak westerlies. It is natural to question whether the conversion of barotropic and/or baroclinic energy is still evident through the interaction between background flow and low-frequency anomalies during the maintenance of UBHs, and that is one of the motivations for the present study.

In the framework of energy conversion, the present study shows that the interference between background flow and low-frequency anomalies is favorable for the maintenance of UBHs by converting both baroclinic energy and barotropic energy to UBHs. In addition, the contributions from transient eddies and diabatic heating are also analyzed. Section 2 introduces the data and methods employed to detect UBHs and diagnoses the contributions from different circulation parts to the energy of the UBHs. Section 3 describes the overall circulation characteristics. Sections 4 and 5 present the main results on the energetics of UBHs. Section 6 provides the main conclusions of this study and further discussion.

## 2. Data and methods

### 2.1 *Datasets and data processing*

The present study uses daily data from Japanese 55-yr Reanalysis (JRA-55; Kobayashi et al., 2015). We analyzed 60 extended winter seasons from 1958 to 2018. The extended winter season refers to the period from November to March of the following year. The horizontal resolution of this dataset is 1.25° × 1.25°. The meteorological variables used in this study include geopotential height, wind velocity, and air temperature. They are distributed on isobaric surfaces. The 2-m air temperature is also utilized to measure the influence of UBHs on the surface weather. All of the abovementioned variables are reanalysis fields based on the assimilation of observational data.

In addition, the diabatic heating field in JRA-55 is also used. It is composed of the large-scale condensation heating rate, convective heating rate, vertical diffusion heating rate, solar radiative heating rate, and longwave radiative heating rate. The large-scale condensation heating rate represents the heating effect by large-scale forced uplift, and the convective heating rate represents the heating effect by cumulus convection. The vertical diffusion heating rate represents the heating effect from the vertical diffusion process. The longwave radiative heating rate and the solar heating rate are the two diabatic heating fields associated with radiation. The parameterization methods for deriving the five diabatic heating rates are described by Kobayashi et al. (2015), and more details can be found in an online document (https://www.jma.go.jp/jma/jma-eng/jma-center/nwp/outline2013-nwp/index.htm).

Blocking highs are characterized by their low-frequency evolution. Accordingly, the present study mainly discusses the energetics of the low-frequency circulation anomalies associated with UBHs. Like Nakamura et al. (1997), we apply the Lanczos filter (Duchon, 1979) with a cut-off frequency of 8 days to isolate the low-frequency circulation from the high-frequency fluctuation. To circumvent the data loss that occurs at the beginning and end of a data sequence when applying the Lanczos filtering procedure with 31 weights, the extended boreal winter period from mid-October to mid-April of the following year is subjected to digital filtering.

Following Nakamura et al. (1997), the local anomaly of a given variable on a particular day is defined as its departure from the local value of the climatological mean annual cycle for the corresponding calendar date. The climatological mean annual cycle is defined as the 60-yr climatological mean daily fields. Note that the 60-yr climatological mean daily fields are further subjected to the 31-day running mean to reduce the day-to-day variability.

### 2.2 *Detection of UBHs*

The detection method of UBHs, based on the method by Tibaldi and Molteni (1990), is almost the same as that of Shi et al. (2020), with minor modifications. First, the large-scale meridional gradient of daily low-frequency

geopotential height ($Z$) at 500 hPa is detected at every longitude,

$$\begin{cases} \text{GHGN} = \dfrac{Z(\varphi_n) - Z(\varphi_0)}{\varphi_n - \varphi_0} \\ \text{GHGS} = \dfrac{Z(\varphi_0) - Z(\varphi_s)}{\varphi_0 - \varphi_s} \end{cases}, \tag{1}$$

where GHGN and GHGS represent the gradients to the north and south of a chosen reference latitude $\varphi_0$, respectively. Here, $\varphi_n = 80°\text{N} + \Delta\varphi$, $\varphi_0 = 60°\text{N} + \Delta\varphi$, and $\varphi_s = 40°\text{N} + \Delta\varphi$, where $\Delta\varphi$ is set from −5° to +5° with an interval of 1.25°. An instantaneous local blocking is considered to occur if GHGN < −10 m degree$^{-1}$ and GHGS > 0 for at least one value of $\Delta\varphi$. Then, a UBH candidate is picked out if the instantaneous local blocking occurs over at least 15 consecutive degrees in longitude and persists for at least 5 days. In addition to the reversal of the large-scale meridional gradient as measured by Eq. (1), the strong anticyclonic anomaly is also considered as an important feature for blocking (Dole and Gordon, 1983; Barriopedro et al., 2010). To ensure that the detected UBHs are associated with strong anticyclonic height anomalies, a UBH event is finally identified if the maximum amplitude of the low-frequency geopotential height anomalies at 500 hPa over the region 55°–80°N, 40°–80°E exceeds +200 gpm at the peak day. The region 55°–80°N, 40°–80°E is around the Ural Mountains. According to our calculation, 53 UBHs are picked out over the 60 winters from 1958 to 2018. The frequency is approximately 0.88 UBHs per winter, which is very close to 0.86 UBHs per winter as identified by Li et al. (2020). Luo et al. (2016a) picked out many more UBHs, i.e., 54 UBHs, during 1979–2013, which might be related to the fact that they do not apply the spatial constraint of 15 degrees for the instantaneous local blocking in the identification of the UBHs. The day with the maximum height anomalies is regarded as the peak day. In the following composite analysis and energy diagnostic analysis, the peak day is regarded as the reference day and denoted as day 0, and day $N$ ($-N$) refers to $N$ days after (before) the peak day.

### 2.3 *Energy budget equations for low-frequency anomalies*

The conventional work on the atmospheric energtics is conducted on a global and integrated sense (Lorenz, 1955). As an extention of Lorenz's work, several local energy budget equations are proposed (Mak and Cai, 1989; Jiang et al., 2013; Liang, 2016; Dai et al., 2021; Zhuge and Tan, 2021a) to explore the dynamics of regional eddies of different temporal and spatial scales (Cai and Mak, 1990; Deng and Mak, 2005; Cai et al., 2007; Jiang et al., 2013; Dai et al., 2021), the Atlantic blocking highs (Ma and Liang, 2017), and atmospheric teleconnection patterns (Tanaka et al., 2016; Zhuge and Tan, 2021a, b). The present study adopts the local KE and APE budget equations for the low-frequency circulation anomalies derived by Tanaka et al. (2016). The detailed derivation is shown in Appendix B of Tanaka et al. (2016), and a brief description on the formulation of the local KE budget equation is given here. It starts from the quasigeostrophic momentum equation. After separating the momentum ($\boldsymbol{V}$) into high-frequency ($\boldsymbol{V}''$) and low-frequency component, the low-frequency component is further decomposed into climatological mean ($\overline{\boldsymbol{V}}$) and anomaly field ($\boldsymbol{V}'$). The tendency equation for $\boldsymbol{V}'$ is firstly obtained by applying low-frequency filtering to the original momentum equation and subtracting the terms regarding the budget of the climatological mean momentum. Finally, the local KE budget equation is readily obtained by multiplying the tendency equation of $\boldsymbol{V}'$ with $\boldsymbol{V}'$. The local APE budget equation is obtained in a similar way but starts from the thermodynamic equation. The budget equations are duplicated in the following with some rearrangement:

$$\frac{\partial(\text{KE})}{\partial t} = \underbrace{\frac{v'^2 - u'^2}{2}\left(\frac{\partial \overline{u}}{\partial x} - \frac{\partial \overline{v}}{\partial y}\right) - u'v'\left(\frac{\partial \overline{u}}{\partial y} + \frac{\partial \overline{v}}{\partial x}\right)}_{\text{CK}_{\text{cli}}} \underbrace{-u'\nabla\cdot(u''\boldsymbol{V}'')' - v'\nabla\cdot(v''\boldsymbol{V}'')'}_{\text{CK}_{\text{TE}}} \underbrace{-\overline{\boldsymbol{V}}\cdot\nabla(\text{KE}) - \boldsymbol{V}'\cdot\nabla(\text{KE})}_{\text{GK}_{\text{adv}}} \underbrace{-\boldsymbol{V}'\cdot\nabla\Phi'}_{\Phi_{\text{adv}}} + \text{RK}, \tag{2}$$

$$\frac{\partial(\text{APE})}{\partial t} = \underbrace{-\frac{RT'}{pS_p}\boldsymbol{V}'\cdot\nabla\overline{T}}_{\text{CP}_{\text{cli}}} \underbrace{-\frac{RT'}{pS_p}\nabla\cdot(\boldsymbol{V}''T'')'}_{\text{CP}_{\text{TE}}} \underbrace{+\frac{R\omega'T'}{p}}_{\text{CP}_{\text{K}}} \underbrace{-\overline{\boldsymbol{V}}\cdot\nabla(\text{APE}) - \boldsymbol{V}'\cdot\nabla(\text{APE})}_{\text{GP}_{\text{adv}}} + \underbrace{\frac{RT'Q'}{pC_pS_p}}_{\text{GP}_{\text{Q}}} + \text{RP}, \tag{3}$$

where the single prime and double prime denote the composite low-frequency anomalies and the high-frequency fluctuation, respectively, associated with the UBHs. The bar denotes the background flow that is obtained as the climatological mean fields. The variables $\text{KE} = (u'^2 + v'^2)/2$ and $\text{APE} = RT'^2/(2pS_p)$ are the kinetic energy and the available potential energy, respectively, for the low-frequency circulation anomalies associated with UBHs; $S_p = R\overline{T}/pC_p - \text{d}\overline{T}/\text{d}p$ is the static stability parameter; $\overline{\boldsymbol{V}} = (u, v)$ is the horizontal wind velocity; and $\Phi$ is the

geopotential. RK in Eq. (2) and RP in Eq. (3) are the residual terms, including the cubic terms associated with the low-frequency anomalies and the various errors in the dataset and the finite differentiation. In the KE budget equation, the term RK also includes the damping effect due to friction force. Note that Eqs. (2) and (3) neglect some terms that are related to the cross-frequency interaction between high- and low-frequency eddies. These terms are assumed to be small which can be inferred from the studies by Dai et al. (2021) on the APE budget analysis of low-frequency eddies. Future studies on other energy budget equations (e.g., Jiang et al., 2013; Liang, 2016; Dai et al., 2021; Zhuge and Tan, 2021a) are needed to obtain a better understanding on the role of cross-frequency eddy–eddy interaction in the maintenance of UBHs.

For the convenience of description and analysis, the terms on the right-hand side of both Eqs. (2) and (3) are grouped. The $CK_{cli}$ and $CK_{TE}$ in Eq. (2) represent the local conversion of the barotropic energy associated with the climatological mean state and transient eddies, respectively. The $GK_{adv}$ and $\Phi_{adv}$ represent the local generation of barotropic energy due to the advection of KE and geopotential energy, respectively. As indicated by Tanaka et al. (2016), $\Phi_{adv}$ in the free atmosphere is composed of the convergence of anomalous ageostrophic geopotential flux $-\nabla_3\cdot(\boldsymbol{V}'_a\Phi')$ and the conversion from APE to KE $(-R\omega'T'/p)$. Here, $\boldsymbol{V}'_a=(u'_a, v'_a, \omega')$ is the ageostrophic wind velocity anomalies and $\nabla_3$ the three-dimensional nabla operator. Note that $-R\omega'T'/p$ will be canceled by $CP_K=\omega'RT'/p$ in Eq. (3). Thus, $\Phi_{adv}+CP_K$ represent the contribution by the convergence of the anomalous ageostrophic geopotential flux. Because we consider KE and APE as a whole, the sum of $\Phi_{adv}$ and $CP_K$ is considered accordingly. The $CP_{cli}$, $CP_{TE}$, and $GP_{adv}$ in Eq. (3) are analogous to $CK_{cli}$, $CK_{TE}$, and $GK_{adv}$ in Eq. (2), respectively, but for the conversions/generations of baroclinic energy. The term $GP_Q$ in Eq. (3) is the generation/dissipation of APE by diabatic heating anomalies.

### 2.4 *Significance test*

The statistical significance of the UBHs composite anomalies is tested based on two-tailed Student's *t* tests at each grid point. To prevent overoptimistic significance results, as pinpointed by Wilks (2016), it is necessary to control the false discovery rate (FDR) in multiple hypothesis tests. The threshold value for the significance level, $p^*_{FDR}$, is determined based on the distribution of ascending sorted *p* values:

$$p^*_{FDR}=\max_{i=1,\ldots,N}[p_{(i)}\leqslant(i/N)\alpha_{FDR}], \tag{4}$$

where $p_{(i)}$ is the *i*th smallest *p* value of all *p* values evaluated at each grid point of composite map north of 20°N, *N* is the total number of grid points, and the control level for the FDR, $\alpha_{FDR}$, is set as 0.05.

## 3. Circulation characteristics of UBHs

To reveal the typical circulation features of UBHs and their impacts on surface air temperature over the Eurasian continent, Fig. 1 shows the composite results of the 500-hPa geopotential height (Z500) anomalies and the 2-m air temperature ($T_{2m}$) anomalies from day −6 to day 6. The Z500 anomalies over the Eurasian continent are marginally significant beyond the period (not shown). On day −6 (Fig. 1a), the significant wave train Z500 anomaly appears over the Eurasian continent with a positive Z500 anomaly over the Ural Mountains and a negative Z500 anomaly over western Europe. The positive Z500 anomaly over the Ural Mountains is elongated zonally and tilts in the northeast–southwest direction to some extent. The circulation anomalies are not significant over the Atlantic (not shown), indicating a large case-to-case variability and no consistent/strong upstream signals. On day −4, the wave train Z500 anomaly is enhanced (Fig. 1b), contributing to anomalous northward advection of warm air mass to its north flank and anomalous southwestward advection of cold air mass to its southeast. Correspondingly, a dipole pattern of significant $T_{2m}$ anomalies appears over the Eurasian continent (Fig. 1i). The significant positive $T_{2m}$ anomaly is located at Barents Sea, while the negative $T_{2m}$ anomaly is anchored over the region from Lake Balkhash to Lake Baikal. The negative Z500 anomaly over western Europe weakens gradually thereafter (Figs. 1b, c) and disappears on day 0 (Fig. 1d). Simultaneously, the positive Z500 anomaly over the Ural Mountains is enhanced and new negative Z500 anomaly emerges and is enhanced and maintained to the southeast of Lake Baikal (Figs. 1c, d), indicating the propagation of a stationary Rossby wave packet over the Eurasian continent. On day 0 (Fig. 1d), the positive Z500 anomaly over Ural Mountains reaches its maximum amplitude of approximately +280 gpm. Consistent with the enhanced Z500 anomalies before the peak day, the intensity of both the primary positive and negative $T_{2m}$ anomalies is enhanced from day −4 to day 0 (Figs. 1i–k). The dipole pattern of $T_{2m}$ anomalies during the evolution of UBHs bears much resemblance to the "warm Arctic/cold Eurasian" pattern (Overland et al., 2010; Luo et al., 2016a).

After the peak day (Figs. 1e–g), the dipole pattern of Z500 anomalies weakens gradually. Note that the significant negative $T_{2m}$ anomaly in the midlatitude region of

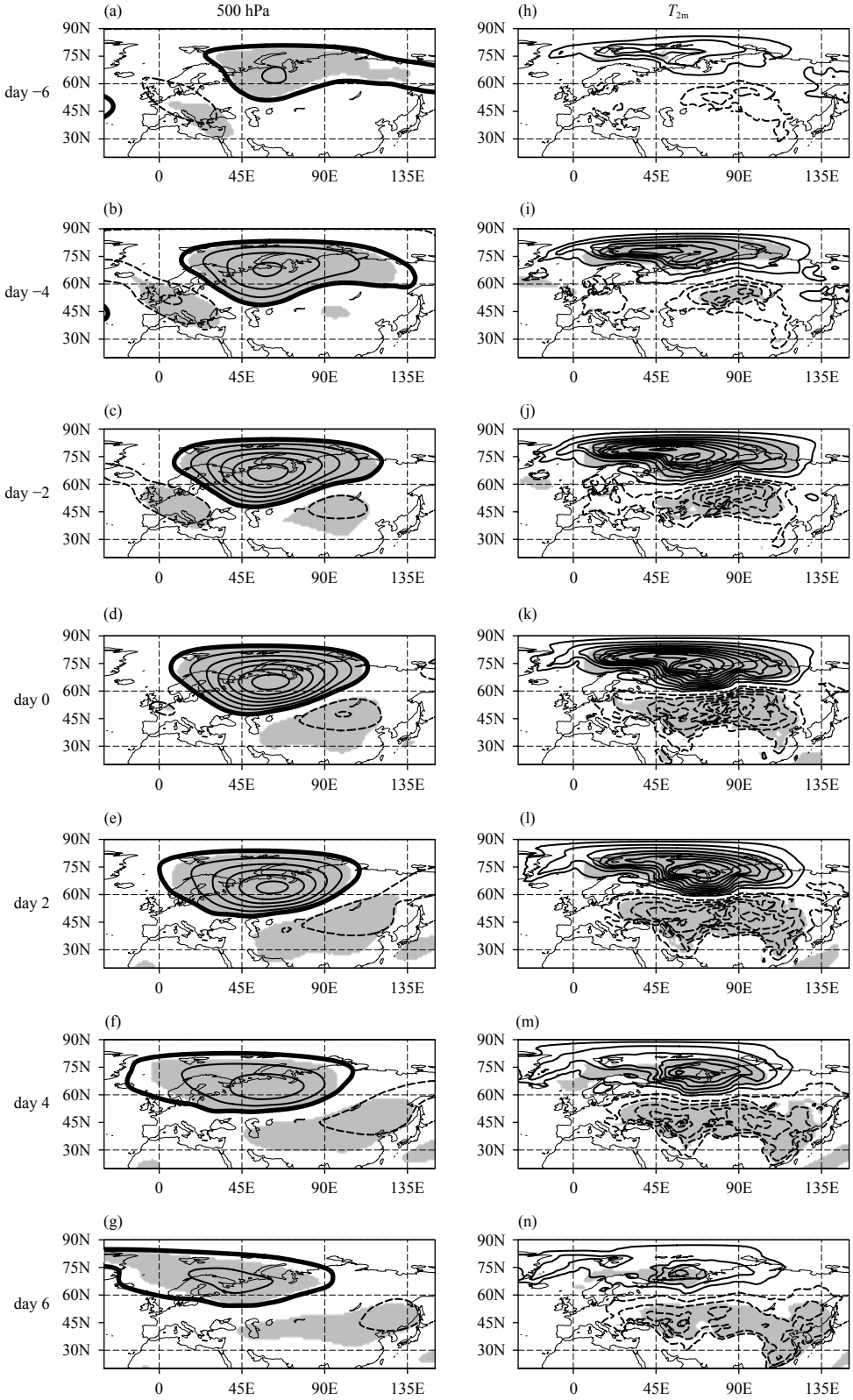


**Fig. 1.** Composite evolution of 53 UBHs: Z500 anomalies (left) and $T_{2m}$ anomalies (right). From top to bottom are day −6, −4, −2, 0, 2, 4, and 6. Contour intervals are 40 gpm for Z500 anomalies and 1 K for $T_{2m}$ anomalies. Solid lines indicate the positive anomalies, and dashed lines the negative anomalies. Zero lines are omitted. Bold contours in (a–g) represent +40 gpm of Z500 anomalies. Shading denotes the statistically significant region at the $\alpha_{FDR} = 0.05$ significance level based on the two-tailed Student's $t$ test. Threshold values for the significance level $p^*_{FDR}$ are 0.005 and 0.004 for the composites of Z500 anomalies and $T_{2m}$ anomalies.

Asia begins to move southeastward along the northeastern side of the Tibetan Plateau, and eastern China is subject to the negative $T_{2m}$ anomaly after day 2 (Figs. 1l–n). Such a southeastward propagation of the $T_{2m}$ anomalies along the Tibetan Plateau was noted by Joung and Hitchman (1982) and Takaya and Nakamura (2005) and it was revealed that it is generally accompanied by the stationary wave trains across the Eurasian continent in the mid- and upper troposphere. It is not surprising to see much resemblance of the UBHs in the present study to the cold-type of Europe–Siberia blocking highs as identified by Shi et al. (2020) in terms of composite Z500 anomalies and $T_{2m}$ anomalies. After all, the cold-type of Europe–Siberia blocking highs identified by Shi et al. (2020) tends to occur around the Ural Mountains.

From Fig. 1d, we can see that the center of positive Z500 anomaly on day 0 is located at approximately 65°N, 60°E. To explore the vertical structure, Figs. 2a and 2c show the vertical cross-sections of the height anomalies on day 0 along 65°N and 60°E, respectively. The UBHs generally exhibit a quasi-barotropic structure throughout the whole troposphere and even the lower stratosphere (Fig. 2a) but tilts slightly northward with height in the middle and lower troposphere (Fig. 2c). The center of the positive height anomalies is located at approximately 250 hPa, and its central amplitude is more than +320 gpm. Figures 2b and 2d show the vertical cross-sections for the air temperature anomalies. Satisfying the hydrostatic balance, the air temperature anomalies around the center of UBHs are positive in troposphere and negative in lower stratosphere, which is consistent with the findings of Cheung et al. (2013). Note that the center of significant positive temperature anomaly is near the ground, which corresponds to the local large conversion of APE. We will discuss this in Section 4.2.

Figure 3 shows the evolution of KE and APE for the composite UBHs. They are shown as the vertically averaged from the surface to 100 hPa. Overall, both KE and APE enhance gradually before day 0 and weaken after day 0. Note that both KE and ΔKE generally achieve their maximum amplitude over the edge of UBHs during their lifecycle, which is associated with the velocity of relatively strong wind occurring over the edge of UBHs. In contrast, both APE and ΔAPE are evident around the center of UBHs, which is associated with the local strong air temperature anomalies or large vertical gradient of anomalous pressure field. Evidently, the spatial distribution of KE and ΔKE is complementary to that of APE and ΔAPE. It inspires us to combine the KE and APE as the total energy to facilitate the discussion on the overall energetics of UBHs.

## 4. Energetics of UBHs

To demonstrate the energetic characteristics, each term on the right-hand side of both Eqs. (2) and (3) is generally averaged horizontally and vertically from surface to 100 hPa. The horizontal average is performed separately over two regions for the sake of comparison. One is the region where the positive height anomalies occur, which

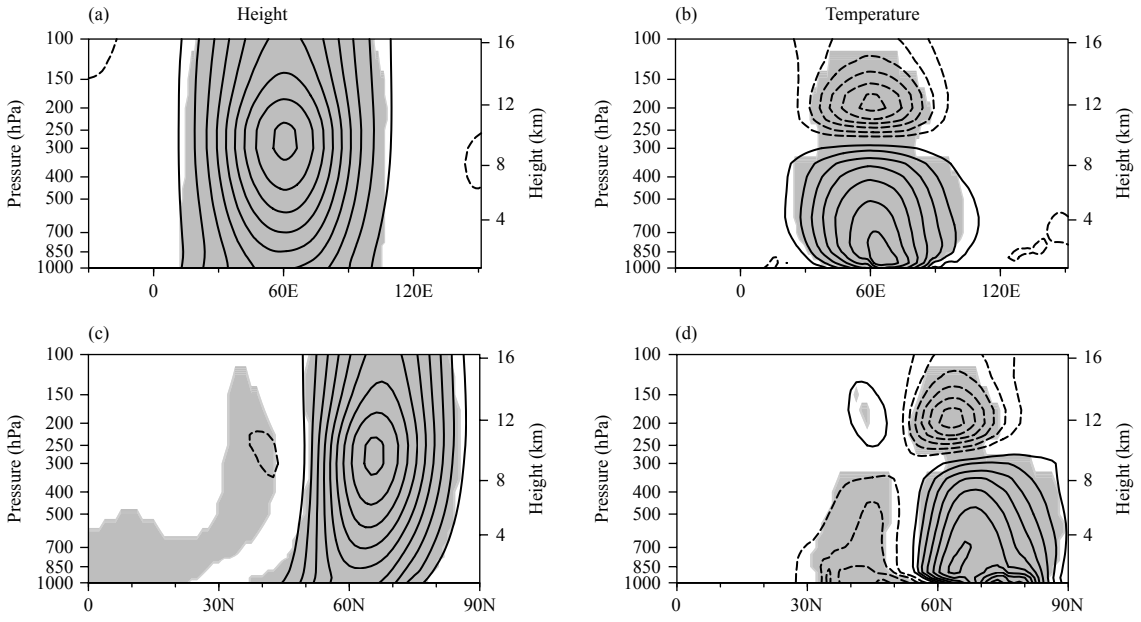


**Fig. 2.** As in Fig. 1, but for vertical cross-sections of (a, c) height anomalies and (b, d) air temperature anomalies on day 0. (a) and (b) are along 65°N, and (c) and (d) are along 60°E.

is identified with the +40 gpm contour (thick solid contour) shown in Figs. 1a–g. Thus, this horizontal average mainly considers the energetics of the anticyclonic anomalies associated with UBHs, which is the same as the method applied to the blocking highs over the Atlantic in Ma and Liang (2017). Hereafter, this region is referred to as UB region for simplicity. Although the area and position of the anticyclonic height anomalies change with time, they overall demonstrate a quasi-stationary feature as seen in Fig. 1. Another average region is broader, i.e., the Eurasian continent (20°–90°N, 0°–120°E). As seen in Fig. 1, UBHs are accompanied by quasi-stationary wave trains over the Eurasian continent. Thus, the average over the Eurasian continent can facilitate the analysis on the energetics of the UBH-related circulation anomalies. In fact, the average is also performed over a fixed region around Ural Mountains (45°–75°N, 40°–90°E), and the final results are not changed qualitatively (omitted).

### 4.1 *Overall characteristics of energy budget*

Figure 4 shows the daily variation of the primary terms of the energy budget equations. The conversion of

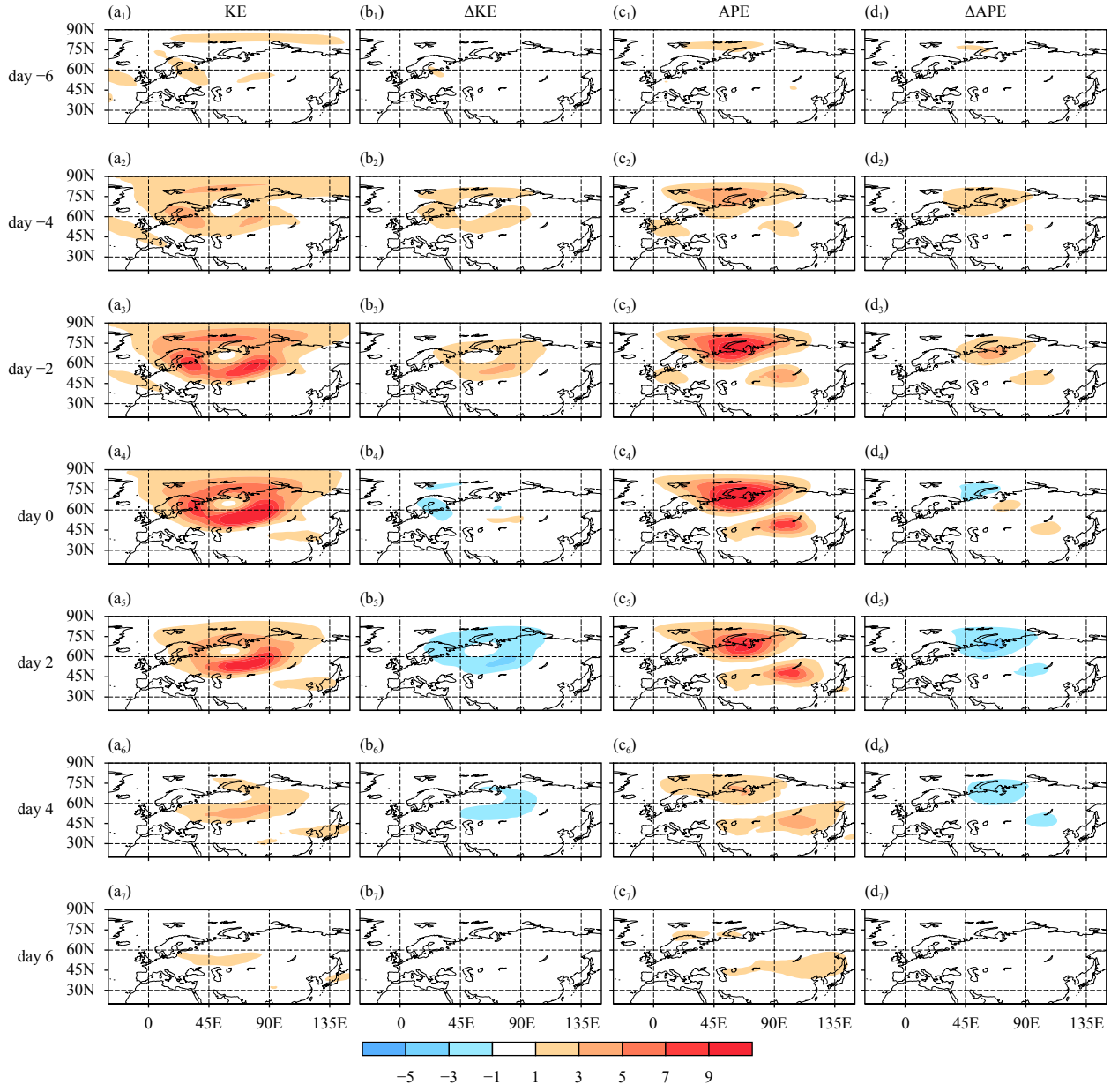


**Fig. 3.** Evolution of KE (first column), change of KE (ΔKE; second column), APE (third column), and change of APE (ΔAPE; fourth column) for the 53 composite UBHs. All terms are averaged from surface ground to 100 hPa. The ΔKE and ΔAPE are calculated through the centered difference. From top to bottom are day −6, −4, −2, 0, 2, 4, and 6. Contour intervals are 10 $m^2\ s^{-2}$ for KE and APE, and 10 $m^2\ s^{-2}\ day^{-1}$ for their changes.

both barotropic energy ($CK_{cli}$) and baroclinic energy ($CP_{cli}$) associated with the background flow is obvious during the evolution of the UBHs (Figs. 4a, b). The amplitude of $CP_{cli}$ is generally stronger than that of $CK_{cli}$, indicating the dominant role of baroclinic energy conversion associated with background flow. The contribution of the convergence of the anomalous ageostrophic geopotential flux $\Phi_{adv} + CP_K = -\nabla\cdot(V'_a\Phi')$ (Fig. 4a) is trivial. Note that there are evident barotropic energy ($CK_{TE}$) and baroclinic energy ($CP_{TE}$) conversions associated with transient eddies. However, $CK_{TE}$ generally has a positive sign while $CP_{TE}$ has a negative one during the lifecycle of UBHs. Therefore, transient eddies exert a two-faceted influence on the maintenance of UBHs. First, they facilitate the KE maintenance of UBHs through barotropic energy conversion; second, they dissipate the APE of UBHs through the baroclinic energy conversion. The diabatic heating is unfavorable for the maintenance of UBHs since it damps the available geopotential energy by generating negative $GP_Q$ (Fig. 4b), which is consistent with the finding by Wang et al. (2021) that the diabatic heating dissipates the wave activity of UBHs.

From the aspect of the lead–lag relationship with the energy tendency of UBHs, it seems that the advection of kinetic energy ($GK_{adv}$) is an important term in modulating the evolution of UBHs (Fig. 4a). Specifically, although its value is small with respect to ΔKE, $GK_{adv}$ is positive mainly from day −6 to day −3 and achieves its maximum value at approximately day −4 which is prior to day −3 when the change of kinetic energy ΔKE achieves its maximum positive value. In addition, after day −3, the value of $GK_{adv}$ gradually decreases and becomes comparable to ΔKE. Note that it reaches its minimum negative value at day 1 which is still prior to day 2 when ΔKE achieves its minimum negative value. The lead–lag relationship between $GK_{adv}$ and ΔKE seems to indicate that KE advection causes the variation of KE of the anticyclonic circulation anomalies over the UB region. Compared with $GK_{adv}$, $CK_{cli}$ has a larger positive value after day −4, but lags behind ΔKE (Fig. 4a). Thus, ΔKE of the anticyclonic anomalies over the UB region at the initial stage might be associated with the KE advection $GK_{adv}$ and the conversion of barotropic energy related with the background flow $CK_{cli}$. With the development of UBHs, the conversion of barotropic energy associated with the background flow $CK_{cli}$ becomes more evident. As for the APE budget, although there is no variation preceding the variation of ΔAPE (Fig. 4b), the baroclinic energy conversion associated with the background flow $CP_{cli}$ into the low-frequency flow is evid-

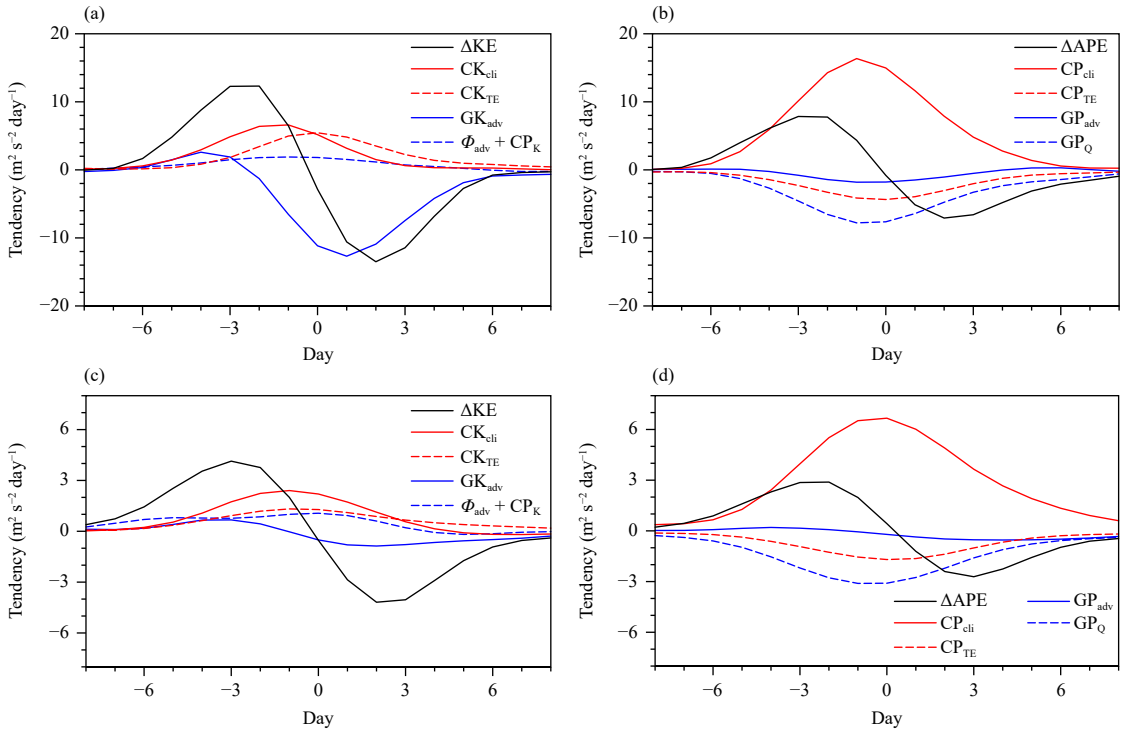


**Fig. 4.** Daily change ($m^2\ s^{-2}\ day^{-1}$) of the primary terms in Eqs. (2) and (3) for the composite UBHs. All terms are averaged from surface ground to 100 hPa and area-weighted averaged over (a–b) the UB region in which the amplitude of the height anomalies is larger than +40 gpm, and (c–d) the region 20°–90°N, 0°–120°E.

ently stronger than other terms including ΔAPE, indicating its dominant role in the maintenance of UBHs. As for transient eddies, no matter whether the conversion of KE ($CK_{TE}$) or APE ($CP_{TE}$) associated with transient eddies into the UBHs, they generally lag behind the ΔKE or ΔAPE for the UBHs, indicating that the low-frequency blocking circulation modulates high-frequency circulation.

If the terms are averaged over the Eurasian region (Figs. 4c, d), the results are basically the same as those averaged over the UB region. However, the amplitude of advection of KE ($GK_{adv}$) has decreased obviously. It means that the KE is mainly redistributed among the circulation anomalies over the Eurasian continent, while the contribution of circulation anomalies outside the Eurasian continent is not obvious.

Overall, there is no strong term prior to the energy variation of UBHs. Thus, the onset mechanism is unclear from our energetic analysis. This study defines the start day as the first day of the reversal of the large-scale meridional gradient of geopotential height. If UBHs are stacked and averaged with respect to the start day, we can find that the strong circulation anomalies already exist on the start day (not shown) and the evolution strongly resembles that shown in Fig. 1 but with approximately 2 days in advance. Thus, it can be expected that the main characteristics of the energy conversion for UBHs based on the composition with respect to the start day are similar to the main results of the present study which mainly reflects the maintenance mechanism of UBHs. To further explore the onset mechanism of UBHs from an energetic perspective, it may require a proper definition of the start day, which deserves future studies.

### 4.2 *Relative importance*

To further measure the relative importance of the primary processes as revealed in the previous subsection, each term in Eqs. (2) and (3) is averaged temporally (Fig. 5). As shown in Fig. 1, the significant large-scale height anomalies appear approximately from day −6 to day 6. Accordingly, the temporal average is applied over the 13-day period. In addition, consistent with the evolution of UBHs (Fig. 1), some energy budget terms change their signs during the 13-day period (Fig. 4). Thus, we further divide the 13-day period into three stages, i.e., developing stage from day −6 to day −3, mature stage from day −2 to day 2, and decay stage from day 3 to day 6. The terms are also averaged over the three sub-periods.

Obviously, the tendency of the total energy (sum of ΔKE and ΔAPE) associated with UBHs is negligible over the 13-day period (Fig. 5a). Nevertheless, both the conversion of barotropic energy ($CK_{cli}$) and baroclinic energy ($CP_{cli}$) associated with the background flow are evidently positive, with the latter being the dominant term over all other terms. The positive values indicate that they are the positive contributors to the maintenance of UBHs. The positive $CP_{cli}$ as well as $CK_{cli}$ is counteracted to a great extent by the consumptions of APE due to diabatic heating (negative $GP_Q$) and by the advection of KE ($GK_{adv}$). The negative $GK_{adv}$ arises from the advection of KE from UBHs to their southeastern region from Lake Balkhash to Lake Baikal (not shown). Note that the primary terms, i.e., $CK_{cli}$, $CP_{cli}$, and $GP_Q$, keep their signs during the whole lifecycle of UBHs, while their amplitude varies with the evolution of UBHs with the maximum value generally observed in the mature stage, which can also be observed in Fig. 4. In contrast, $GK_{adv}$ is slightly positive during the developing stage and turns evidently negative during the decay stage. As for transient eddies, both KE conversion ($CK_{TE}$) and APE conversion ($CP_{TE}$) have an amplitude comparable to $CK_{cli}$ (Figs. 5a, e), especially during the mature stage (Figs. 5c, g). It indicates that transient eddies play an important role in maintaining the energy budget balance of UBHs. Due to the opposite signs between $CK_{TE}$ and $CP_{TE}$, however, the net contribution from transient eddies is marginal. The net contribution from the advection of APE ($GP_{adv}$) and the term $\Phi_{adv} + CP_K$ is trivial to the maintenance of the whole circulation anomalies of UBHs. It should be pointed out that as is seen in Wang et al. (2021), if we analyze the different parts of UBHs instead of considering them as a whole, the effects of these two terms are obvious. Specifically, $GP_{adv}$ advects APE from the western part of UBHs to the eastern part, while the anomalous ageostrophic geopotential flux ($\Phi_{adv} + CP_K$) becomes convergent over the western and eastern parts of UBHs and divergent over the central to northeast part (not shown). Such energy transportation among different parts of UBHs is not discussed in the present study. Instead, we put more emphasis on the energy conversion among different circulation components (i.e., climatological mean state, low-frequency anomalies, and high-frequency anomalies). Accordingly, both $GP_{adv}$ and $\Phi_{adv} + CP_K$ will not be discussed in the following text.

If horizontal average is performed over the broader region, i.e., the Eurasian continent (second row of Fig. 5), the relative importance of each term is not changed much, except for the advection of the barotropic energy ($GK_{adv}$) (Fig. 5e) that is reduced to a great extent. Thus, the maintenance of UBHs is characterized by the balance to a great extent between the two positive contributors, i.e., conversions of baroclinic energy and barotropic energy associated with the background, energy conver-

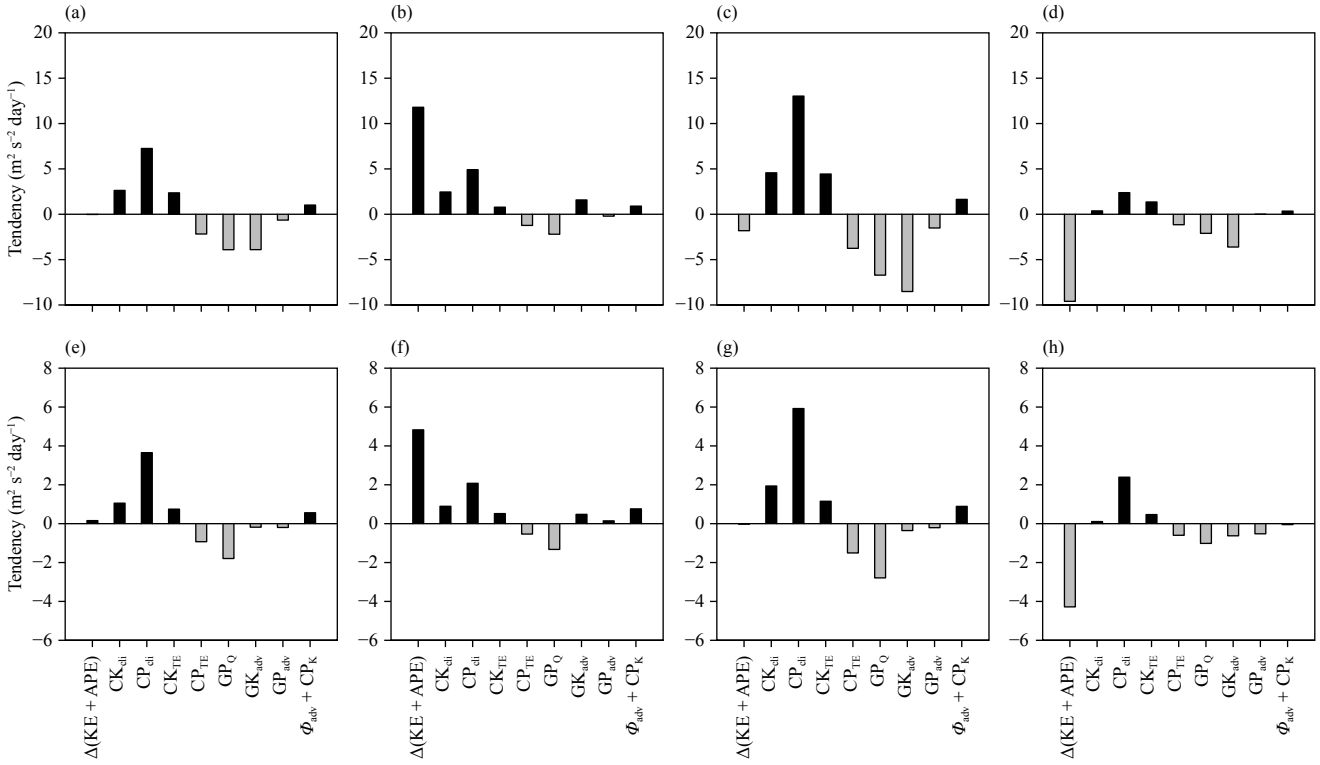


**Fig. 5.** Tendency (m$^2$ s$^{-2}$ day$^{-1}$) of total energy (ΔKE + ΔAPE) and each term in Eqs. (2) and (3) for the composite UBHs. First column shows the results averaged from day −6 to day 6, second column from day −6 to day −3, third column from day −2 to day 2, and last column from day 3 to day 6. All terms are averaged from surface ground to 100 hPa and area-weighted averaged over (a–d) the UB region in which the amplitude of the height anomalies is larger than +40 gpm, and (e–h) the region 20°–90°N, 0°–120°E.

sion associated with transient eddies, and the negative contributor, i.e., the diabatic heating.

Figure 6 shows the vertical profiles of the primary terms which are averaged from day −6 to day 6 and area-weighted averaged horizontally over the UB region (Fig. 6a) and Eurasian continent (Fig. 6b). Obviously, the dominant conversion of baroclinic energy associated with background flow ($CP_{cli}$) is evident mainly in the middle and lower troposphere (Figs. 6a, b). Note that $CP_{cli}$ decreases linearly with height below 850 hPa, which is associated with air temperature anomalies with relatively large amplitude in the lower troposphere (Fig. 1) as well as large gradient of the background air temperature (shown latter). Likewise, the generation of APE due to diabatic heating ($GP_Q$) has its minimum negative values in the middle and lower troposphere. In contrast, the conversion of barotropic energy associated with background flow ($CK_{cli}$) contributes positively in the upper troposphere (Figs. 6a, b). Although the barotropic energy conversion associated with transient eddies ($CK_{TE}$) contributes positively in the upper troposphere, the baroclinic energy conversion from transient eddies ($CP_{TE}$) contributes negatively in the middle and lower troposphere (Figs. 6a, b), consistent with the results revealed by Jiang et al. (2013) and Dai et al. (2021) about the roles of high-frequency eddies in the energetics of low-frequency circulation in the Northern Hemisphere.

The relatively large negative values of the advection term of barotropic energy ($GK_{adv}$) in the upper troposphere (Fig. 6a) mean that a large amount of barotropic energy is transported out of the anticyclonic anomalies that mainly occur during mature and decay stages (not shown). If the horizontal average is performed over the Eurasian continent (Fig. 6b), the amplitude of $GK_{adv}$ is reduced dramatically.

## 5. Reasons from circulation configurations

As revealed in the previous section, $CP_{cli}$, $CK_{cli}$, and $GP_Q$ are the primary terms for the energy budget of UBHs. Section 2.3 shows that $CK_{cli}$ and $CP_{cli}$ represent the energy conversion due to the interference between the low-frequency circulation anomalies and background flow, while $GP_Q$ is determined by low-frequency air temperature anomalies and diabatic heating anomalies. Thus, exploring the circulation configurations is helpful for understanding the energetic characteristics of UBHs. Note that the three terms vary slowly and keep their signs during the lifecycle of UBHs (not shown), which can be inferred from Fig. 4. It is not surprising to see such a simil-

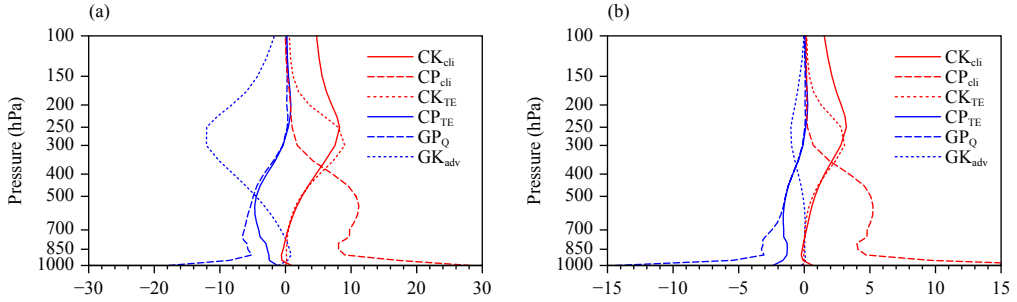


**Fig. 6.** Vertical profile of the primary terms ($10^{-5}$ m$^2$ s$^{-3}$) in Eqs. (2) and (3) for the composite UBHs. These terms are obtained by averaging temporally from day −6 to day 6 and area-weighted averaging over (a) UB region (bounded by +40 gpm contours of height anomalies) and (b) 20°–90°N, 0°–120°E.

arity because low-frequency circulation anomalies (e.g., $u'$, $v'$, and $T'$) are used in the evaluation of energy terms. Accordingly, this section averages these terms over the 13-day period from day −6 to day 6 to show the main energetics results.

### 5.1 *Barotropic energy conversion associated with background flow ($CK_{cli}$)*

The horizontal structure of barotropic energy conversion ($CK_{cli}$) is further discussed via $CK_{cli}$ at 250 hPa where $CK_{cli}$ is the most evident as revealed in Fig. 6. As shown in Fig. 7, the large values of $CK_{cli}$ mainly appear around the UB region. Positive $CK_{cli}$ is located at the southeastern and northern parts of UBHs, while negative $CK_{cli}$ at the eastern, southern, and western parts of UBHs. Since both the area and amplitude of positive $CK_{cli}$ are larger than those of negative $CK_{cli}$, net positive $CK_{cli}$ is obtained over the UB region or the Eurasian continent (20°–90°N, 0°–120°E) (Fig. 6). Then, we need to further discuss how the positive $CK_{cli}$ is formed, especially over the northern and southeastern parts of the UBHs.

The term $CK_{cli}=\frac{v'^2-u'^2}{2}(\frac{\partial\overline{u}}{\partial x}-\frac{\partial\overline{v}}{\partial y})-u'v'(\frac{\partial\overline{u}}{\partial y}+\frac{\partial\overline{v}}{\partial x})$ is the scalar product of $\boldsymbol{E}=(\frac{v'^2-u'^2}{2},-u'v')$ and $\boldsymbol{D}=(\frac{\partial\overline{u}}{\partial x}-\frac{\partial\overline{v}}{\partial y},\frac{\partial\overline{u}}{\partial y}+\frac{\partial\overline{v}}{\partial x})$. Note that $\boldsymbol{E}$ is not identical to the horizontal component of the extended E–P flux proposed by Hoskins et al. (1983) and Trenberth (1986). The extended E–P flux takes a time mean form, i.e., $(\overline{\frac{v'^2-u'^2}{2}},-\overline{u'v'})$, and thus can be used to evaluate the feedback of eddies onto the basic (time average) flow through the convergence of the fluxes. Without the climatological average, $\boldsymbol{E}=(\frac{v'^2-u'^2}{2},-u'v')$ herein is not suitable for the evaluation of such feedback of eddies.

In fact, $\boldsymbol{E}$ and $\boldsymbol{D}$ are associated with the configuration of circulation anomalies and basic flow, respectively. Accordingly, $CK_{cli}$ can be further explored in terms of the configurations of both UBHs and basic flow. For the meridionally/zonally elongated anomalies, $\boldsymbol{E}$ mainly points to the zonal direction ($|\frac{v'^2-u'^2}{2}|\gg|-u'v'|$), while for the tilted anomalies, $\boldsymbol{E}$ has an evident meridional component ($|\frac{v'^2-u'^2}{2}|\sim|-u'v'|\neq 0$) (Cai et al., 2007). Like the zonally elongated anomalies, e.g., Pacific/Japan teleconnection pattern (Kosaka and Nakamura, 2006) and western Pacific atmospheric teleconnection pattern (Tanaka et al., 2016), UBHs also exhibit a zonally elongated structure with a dominant zonal-pointing $\boldsymbol{E}$ (arrows in the first column of Fig. 7). The tilted circulation anomalies in the southeastern and southwestern parts of the UBHs correspond to the local $\boldsymbol{E}$ with an evident meridional component. As for $\boldsymbol{D}$, its two components depict the stretching and shearing deformation of the basic flow, respectively. To further discuss the formation of $CK_{cli}$, $CK_{cli}$ is decomposed into $CK_{cli\_x}=\frac{v'^2-u'^2}{2}(\frac{\partial\overline{u}}{\partial x}-\frac{\partial\overline{v}}{\partial y})$ and $CK_{cli\_y}=-u'v'(\frac{\partial\overline{u}}{\partial y}+\frac{\partial\overline{v}}{\partial x})$. Here, only the climatological mean westerlies are discussed since the influence from the southerlies is relatively negligible.

As shown in Fig. 7c, the positive $CK_{cli}$ mainly comes from $CK_{cli\_y}$; $CK_{cli\_y}$ is the strongest over the southeastern part of UBHs. First, $\boldsymbol{E}$ has an evident southward-pointing component over this region. Second, the climatological mean isoline of 16 m s$^{-1}$ extends northward over the longitudinal sector 70°–105°E, forming the local large southward gradient of the climatological mean westerlies around 60°N (Fig. 7a). The superimposition of southward-pointing $\boldsymbol{E}$ onto the southward gradient of the climatological mean westerlies leads to the relatively large positive $CK_{cli\_y}$. As for the positive $CK_{cli}$ over the northern part of UBHs (Fig. 7a), both $CK_{cli\_x}$ and $CK_{cli\_y}$ contribute positively. The isolines of the climatological mean westerlies tilt in the northwest–southeast direction, forming its southwestward gradient and leading to its

local confluence ($\frac{\partial \overline{u}}{\partial x} < 0$) and southward gradient ($\frac{\partial \overline{u}}{\partial y} < 0$). Under such a circumstance, the westward-pointing $\boldsymbol{E}$ over the northern part of UBHs leads to the local positive $CK_{cli\_x}$ (Fig. 7b), while $\boldsymbol{E}$ with a slightly southward-pointing component over the northwestern part of UBHs leads to local positive $CK_{cli\_y}$ (Fig. 7c).

To sum up, the interference between the background flow and low-frequency anomalies is conducive to the positive conversion of barotropic energy into UBHs. The climatological mean westerlies have a large southward gradient to the north of Lake Balkhash and a southwestward gradient around Barents Sea. Such a background flow can facilitate the positive conversion of barotropic energy over the Eurasian continent when it interferes with UBHs.

### 5.2 *Baroclinic energy conversion associated with background flow ($CP_{cli}$)*

Unlike the evident $CK_{cli}$ in the upper troposphere and lower stratosphere, the baroclinic energy extraction from background flow $CP_{cli}$ mainly occurs in the middle and lower troposphere. Note that $CP_{cli}$ has a local maximum at 500 and 1000 hPa and a local minimum at 850 hPa (Fig. 6), implying the difference in the formation of the positive $CP_{cli}$ above and below 850 hPa. Accordingly, $CP_{cli}$ at 500 and 1000 hPa is analyzed separately.

As seen in Fig. 7d, the positive and negative $CP_{cli}$ at 500 hPa are aligned from Kara Sea to the western North Pacific with gradually decreasing amplitude. Within the UB region, the conversion of baroclinic energy associated with the background flow is evident over the western parts of UBHs while the reverse situation occurs over the eastern parts. The former is stronger than the latter, leading to the net conversion of baroclinic energy associated with the background flow into the UBHs.

As shown in Section 5.1, $CP_{cli}$ is further decomposed into zonal component $CP_{cli\_x} = -\frac{Ru'T'}{pS_p}\frac{\partial T}{\partial x}$ and meridional component $CP_{cli\_y} = -\frac{Rv'T'}{pS_p}\frac{\partial T}{\partial y}$. Hereafter, $(-u'T', -v'T')$ is referred to as the anomalous temperature flux although there is a negative sign before the "real" anomalous temperature flux. Clearly, the anomalous temperature flux exhibits a cyclonic feature within the UB region (Figs. 7d, g). Note that the spatial distribution of the pos-

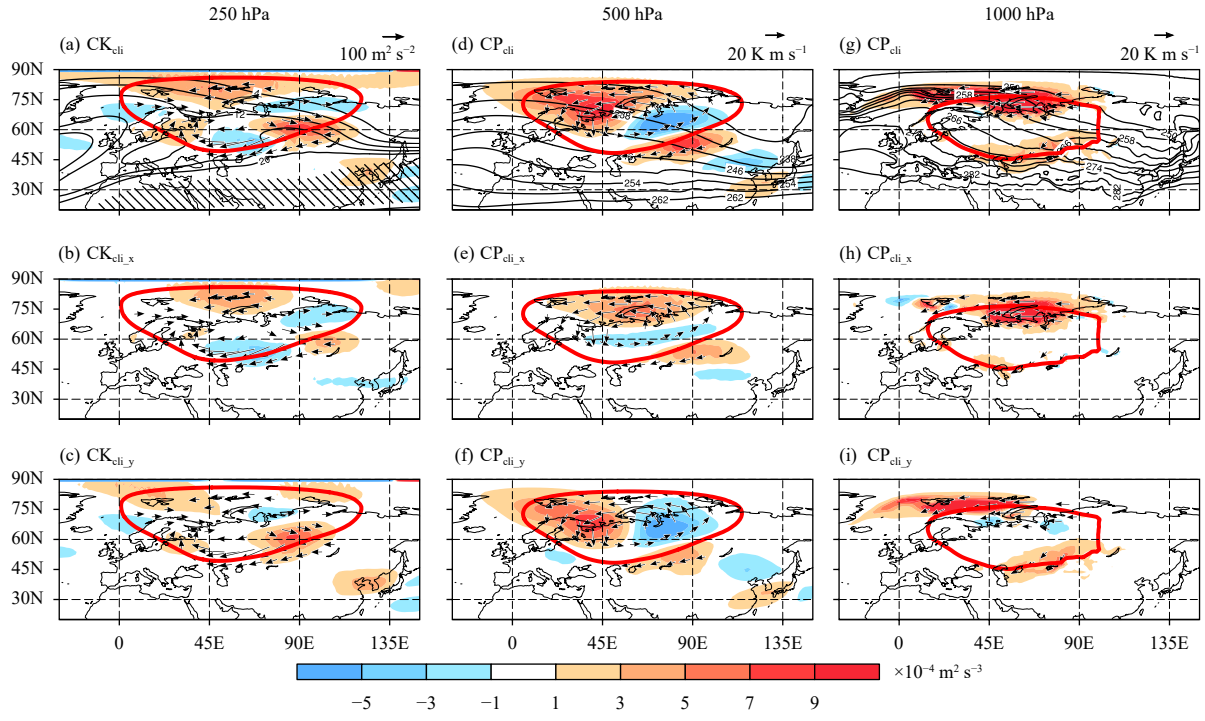


**Fig. 7.** (a) Extraction of barotropic energy from background flow ($CK_{cli}$) at 250 hPa (shading) averaged from day −6 to day 6. (b) $CK_{cli\_x}$ and (c) $CK_{cli\_y}$ are the zonal and meridional components of $CK_{cli}$, respectively. (d) Extraction of the baroclinic energy from the background flow ($CP_{cli}$) at 500-hPa level (shading). (e) $CP_{cli\_x}$ and (f) $CP_{cli\_y}$ are the zonal and meridional components of $CP_{cli}$, respectively. (g–i) As in (d–f), but at 1000 hPa. Shading interval is $2 \times 10^{-4}$ m$^2$ s$^{-3}$. Black contours in (a) represent the climatological-mean zonal wind at 250 hPa (contoured every 4 m s$^{-1}$, beginning at 4 m s$^{-1}$) in boreal winter, and in (d) and (g) represent the climatological-mean air temperature (contoured every 4 K, beginning at 234 and 250 K). Arrows in (a–c) are $\boldsymbol{E}$ (m$^2$ s$^{-2}$) at 250-hPa level, and (d–f) anomalous temperature flux $(-u'T', -v'T')$ (K m s$^{-1}$) at the corresponding level. Red contours represent +40 gpm of composite height anomalies at the corresponding level to indicate the region where the strong anticyclonic circulation anomalies anchor.

itive height anomalies associated with UBHs is asymmetric. Specifically, the height anomalies extend more zonally in their northern part than its southern part (thick contour in Fig. 1 or 7), which could be also observed in the Ural–Siberia blocking high (Cheung et al., 2013) or the Europe–Siberia blocking high (Shi et al., 2020). Accordingly, the anomalous westerlies and the related zonal component of the anomalous temperature flux are more evident in the northern part of UBHs than those in the southern part. Note that, like the southwestward gradient of the climatological mean westerlies (Fig. 7a), the climatological mean air temperature also has a southwestward gradient from the northeastern Atlantic to the middle latitude of East Asia. Interfering with the southwestward gradient of the background flow, the cyclonically rotating temperature flux produces positive $CP_{cli\_x}$ with stronger amplitude over the northern part of UBHs than the negative counterpart over the southern part of UBHs (Fig. 7e). Meanwhile, a zonal dipole $CP_{cli\_y}$ within the UB region has positive values over the western part of UBHs and negative ones of comparable amplitude over the eastern part of UBHs. Therefore, it is the strong conversion of baroclinic energy over the northern part of UBHs ($CP_{cli\_x}$) that contributes to the net conversion of baroclinic energy into UBHs. In addition, there is another region with evident conversion of baroclinic energy associated with background flow, i.e., the region from Aral Sea to Lake Baikal. It is associated with the anomalous northeasterlies and the negative air temperature anomalies to the southeast of the UBHs (not shown).

At 1000 hPa, the air temperature flux is evident over the northern flank of the UB region with a westward pointing and over the southern flank of the UB region with a southwestward pointing. Note that the gradient of the climatological mean air temperature is much stronger at 1000 hPa (Fig. 7g) than that at middle troposphere (Fig. 7d), especially over the region from the northeastern Atlantic to Kara Sea. Under such a circumstance, there are strong positive $CP_{cli}$ around the northern flank of UBHs and modest positive $CP_{cli}$ around the southern flank of UBHs (Fig. 7g). The $CP_{cli\_x}$ accounts for the largest proportion of the $CP_{cli}$ around the Kara Sea (Fig. 7h), while $CP_{cli\_y}$ contributes to the formation of positive $CP_{cli}$ around the northwestern and southeastern flanks of the UB region (Fig. 7i). The negative $CP_{cli}$ is negligible over the whole Eurasian continent. Accordingly, the net $CP_{cli}$ over the UB region or the Eurasian continent at 1000 hPa is larger than that in the middle troposphere (as seen in Fig. 6).

Note that the spatial distribution of $CP_{cli}$ at 1000 hPa strongly resembles that of $T_{2m}$ anomalies (Fig. 1h), implying the positive contribution of surface air temperature anomalies to the maintenance of the UBHs. As revealed in Section 3, the formation of surface air temperature anomalies is in turn associated with the circulation anomalies associated with UBHs. Therefore, the maintenance of UBHs and that of the air temperature anomalies in the lower troposphere are coupled, facilitating the persistence of UBHs. As for the minimum $CP_{cli}$ at 850 hPa (Fig. 6), it is associated with the fact that air temperature flux gradually enhances with height while the climatological mean air temperature gradient weakens with height (not shown).

Analogous to the climatological mean westerlies, the climatological mean air temperature has evident southwestward gradient around the Kara Sea and Lake Balkhash in the mid- and lower troposphere. The conversion of baroclinic energy becomes positive to the UBHs when the anomalous temperature flux interferes with the background flow.

### 5.3 *Baroclinic energy generation due to diabatic heating ($GP_Q$)*

Previous studies revealed that the diabatic heating is important to the maintenance of blocking highs (Cheung et al., 2013; Pfahl et al., 2015) and atmospheric teleconnection pattern (Kosaka and Nakamura, 2006; Kosaka et al., 2009; Tanaka et al., 2016). Motivated by these studies, the influence of diabatic heating on the UBHs is discussed in the energetics framework, i.e., the generation of APE by anomalous diabatic heating ($GP_Q$).

According to the vertical profile of $GP_Q$ (Fig. 6), the negative $GP_Q$ achieves its local maximum amplitude at approximately 700 and 1000 hPa. Figure 8 shows the horizontal distribution of $GP_Q$ at these two isobaric levels. At 1000 hPa (Fig. 8b), the evident negative $GP_Q$ is mainly located at the region from Barents Sea to Kara Sea and around Caspian Sea. These regions are roughly characterized by positive $T_{2m}$ anomalies (Figs. 1i–n) and anomalous diabatic heating with an opposite sign (Fig. 9f). Specifically, the positive $T_{2m}$ anomalies from Barents Sea to Kara Sea (Figs. 1i–n) are accompanied by the negative diabatic heating anomalies (Fig. 9f), while the negative $T_{2m}$ anomalies around Caspian Sea are accompanied by the positive diabatic heating anomalies, both of which lead to the formation of negative $GP_Q$ (Fig. 8b). Although the positive $GP_Q$ is also discernable, its spatial coverage and intensity are apparently less than those of negative $GP_Q$. Thus, the near-ground air temperature anomalies overall are damped by the anomalous diabatic heating, leading to the dissipation of APE of UBHs near the ground.

If the diabatic heating rate is decomposed, we can find that the anomalous longwave radiation heating (Fig. 9g) and anomalous vertical diffusion heating (Fig. 9h) are the two main contributors to the diabatic heating anomalies at 1000 hPa. In fact, the damping effect of the anomalous vertical diffusion heating decreases with height. At 950 hPa (Fig. 9e), the anomalous vertical diffusion heating rate becomes weaker but still has a negative sign over Barents Sea. However, it becomes positive over western Siberia (Fig. 9e), acting as a contributor to the maintenance of the local positive air temperature anomalies (not shown). The negative longwave radiative heating anomalies centered at Barents Sea at 1000 hPa (Fig. 9g) expand to Kara Sea and western Russia at 950 hPa (Fig. 9d). Thus, the combined effect of the longwave radiative heating and vertical diffusion heating has a damping effect over the UB region or the Eurasian continent.

The evident negative $GP_Q$ anomalies at 700 hPa (Fig. 8a) are similar to those at 1000 hPa. They mainly appear within the UB region but become weaker than its counterpart at 1000 hPa (Fig. 8b). It can damp the positive air temperature anomalies in situ (not shown). Note that the significant negative large scale condensation heating (Fig. 9b) becomes the main contributor to the diabatic heating anomalies. In fact, UBHs can inhibit the large scale precipitation within the UB region (not shown), which induces the negative diabatic heating anomalies and further the negative diabatic heating anomalies. Therefore, the formation of diabatic heating anomalies at 700 hPa is different from that at 1000 hPa. Above 700 hPa, the diabatic heating anomalies decrease with height (Fig. 6).

## 6. Conclusions and discussion

Based on the composite analysis, the energy budget equations are utilized to analyze the maintenance mechanism of UBHs. The analysis is conducted not only over the Ural Mountains where the strong anticyclonic anomalies anchor but also over the Eurasian continent where the wave train anomalies are evident. To summarize the energetics of UBHs, Fig. 10 shows a schematic diagram of the primary energy conversion processes that are evident in the energy budgets of UBHs. It is found that the conversions of barotropic and baroclinic energy associated with the background flow, i.e., positive $CK_{cli}$ and positive $CP_{cli}$, are the dominant positive contributors to the maintenance of UBHs. The $CK_{cli}$ achieves its maximum amplitude in the upper troposphere, and $CP_{cli}$ in the middle and lower troposphere. In addition, the advection of KE is prior to the variation of KE of UBHs,

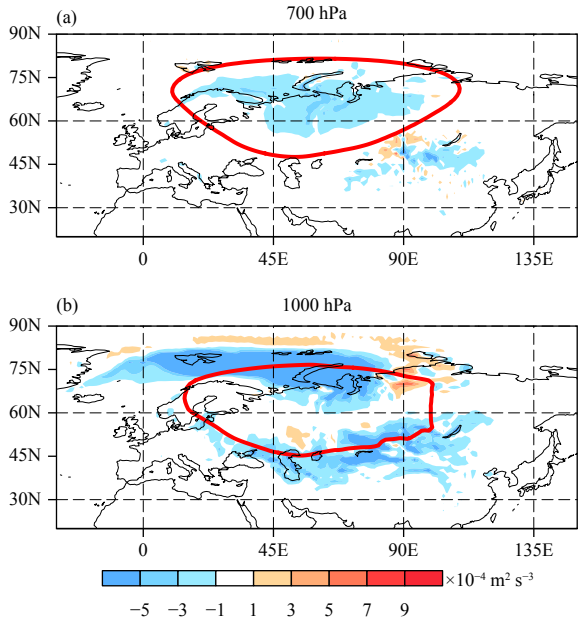


**Fig. 8.** As in Fig. 7, but for the generation of APE by anomalous diabatic heating ($GP_Q$) at (a) 700 hPa and (b) 1000 hPa. Contour interval is $2 \times 10^{-4}$ m$^2$ s$^{-3}$.

indicating that the former is an important indicator of the latter. However, the contribution of the KE advection term to the energy budget balance of UBHs will be greatly reduced if the wave train anomalies across the entire Eurasian continent associated with UBHs are considered as a whole.

The reason for positive $CP_{cli}$ is further explored through the configurations of background flow and low-frequency circulation anomalies associated with UBHs. In the middle and lower troposphere, first, the background air temperature has an overall southwestward gradient; second, UBHs induce strong westward-pointing temperature flux over the northern part of strong anticyclonic height anomalies of the UBHs, which is consistent with the asymmetry in structure of the UBHs that is more zonally elongated in their northern part than their southern part. It induces the local positive $CP_{cli}$ over the northern part of the UBHs. Combined with another positive $CP_{cli}$ to the southeast of the strong anticyclonic height anomalies, the positive $CP_{cli}$ over the UB region or Eurasian continent is dominant during the lifecycle of UBHs. Note that the surface air temperature anomalies induced by UBHs correspond to the large value of $CP_{cli}$, implying a self-sustained mechanism for the UBHs via the interference between background flow and UBHs. As for $CK_{cli}$, its positive value mainly occurs over the northwest of Lake Baikal where the southward pointing $\boldsymbol{E} = (\frac{v'^2 - u'^2}{2}, -u'v')$ of UBHs superimposes onto the south-

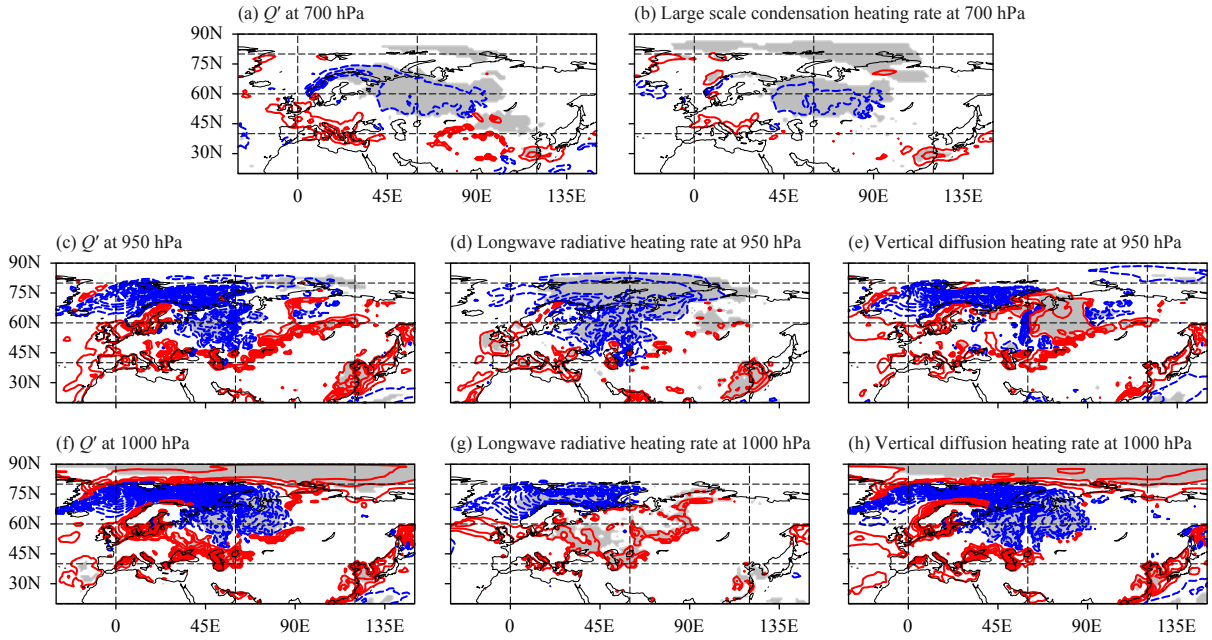


**Fig. 9.** (a) Anomalous diabatic heating at 700 hPa which is the sum of five anomalous diabatic heating rate terms. (b) Anomalous large-scale condensation heating rate at 700 hPa. (c) Same as (a), but at 950 hPa. (d) Anomalous longwave radiation heating rate and (e) anomalous vertical diffusion heating rate at 950 hPa. (f–h) Same as (c–e), but at 1000 hPa. Red solid lines represent positive anomalies, and blue dashed lines negative anomalies. Units: K day$^{-1}$. Shading denotes the statistically significant region at $\alpha_{FDR} = 0.05$ significance level based on the two-tailed Student's $t$ test.

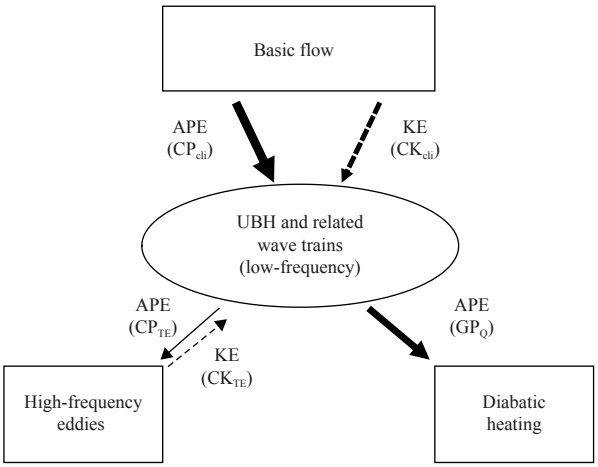


**Fig. 10.** Schematic diagram for the primary energy conversions among different circulation components. The directions of arrows indicate the directions of the energy conversion, while the thickness of the arrows indicate qualitatively the amplitude of the energy conversion. The solid and dashed arrows represent the conversions of APE and KE, respectively. The terms in the energy budget equations which are associated with the primary energy conversions are shown in the brackets.

ward gradient of the background westerlies. Therefore, the interference between background flow and low-frequency anomalies is conducive to the maintenance of UBHs.

In contrast, the diabatic heating anomalies tend to damp the APE in the middle and lower troposphere during the lifecycle of UBHs. Due to longwave radiation and vertical diffusion heating anomalies, the negative diabatic heating anomalies appear near the ground over the region from Barents Sea to western Russia. They tend to damp local positive air temperature anomalies and form negative $GP_Q$. In addition, evident negative large scale condensation heating anomalies appear around 700 hPa, which is associated with the reduction of precipitation around the Ural Mountains. It is also unfavorable for the local positive air temperature anomalies and thus forms the negative $GP_Q$. Therefore, the diabatic heating anomalies are not favorable for the maintenance of UBHs, which is consistent with the finding by Wang et al. (2021). Cheung et al. (2013) stated that the diabatic heating is favorable for the maintenance of Ural–Siberia blocking highs. It is not surprising to see the difference in the role of diabatic heating between our results and theirs. They emphasize the total fields while we emphasize the anomaly fields associated with the UBHs.

It can be inferred from the lead–lag relation that the high-frequency transient eddies are modulated by the low-frequency blocking circulation. The feedback of transient eddies has dual effects on the UBHs (Fig. 10). First, they facilitate the maintenance of UBHs via the positive conversion of KE associated with the transient eddies to UBHs (positive $CK_{TE}$) mainly in the middle

and upper troposphere. On the other hand, the conversion of APE to transient eddies occurs in the lower troposphere (negative $CP_{TE}$). The small net contribution of transient eddies due to their two-faceted role is consistent with the net marginal contribution of transient eddies in the maintenance of the UBHs (Li, 2004; Luo et al., 2016b; Shi et al., 2020). However, due to the comparable amplitude of either $CK_{TE}$ or $CP_{TE}$ to that of $CK_{cli}$, transient eddies are important in maintaining the energy budget balance of UBHs.

For the sake of comparison, the same method is also applied to the blocking highs over the North Atlantic (Fig. 11). Similar to the UBHs, the conversion of baroclinic energy associated with the background flow is also the primary positive contributor to the maintenance of the blocking highs over the North Atlantic. In addition, the diabatic heating also tends to damp the energy of the blocking highs. Nevertheless, there are two differences in the energetics between UBHs and the blocking highs over the North Atlantic. The first one is the contribution from transient eddies. Consistent with the active storm tracks over the North Atlantic, the barotropic energy conversion from transient eddies ($CK_{TE}$) becomes more evident. Accordingly, transient eddies contribute relatively more ($CK_{TE}$ + $CP_{TE}$) to the maintenance of the blocking highs over the North Atlantic than they do to UBHs. Thus, the result is consistent with the previous studies that transient eddies facilitate the maintenance of the blocking highs over the North Atlantic. The second difference is the barotropic energy conversion associated with background flow ($CK_{cli}$). The $CK_{cli}$ is marginally positive for the circulation anomalies over the whole North Atlantic (Fig. 11b) or even negative (Fig. 11a) for the strong anticyclonic circulation anomalies. In fact, the $\boldsymbol{E}$ vectors are similar between UBHs and the blocking highs over the North Atlantic, while the climatological mean westerlies have a southeastward gradient over the northeast Atlantic (not shown) which is different from the southwestward gradient around Barents Sea (Fig. 7a). Therefore, such a difference in $CK_{cli}$ between UBHs and the blocking highs over the North Atlantic is attributable to different configurations of the climatological mean westerlies.

Ma and Liang (2017) pinpointed that the local energy of low-frequency circulation (denoted as $KE_{low}$ and $APE_{low}$) is not equal to the energy derived from subtracting the local energy of high-frequency circulation from that of the total circulation (denoted as $KE_{total\text{-}high}$ and $APE_{total\text{-}high}$). Applying the horizontal average onto the energy might mitigate such differences. To verify this speculation, Table 1 shows the $KE_{total\text{-}high}$ and $APE_{total\text{-}high}$, the percentage of $KE_{low}$ to $KE_{total\text{-}high}$, and the percentage of $APE_{low}$ to $APE_{total\text{-}high}$, respectively, all of which are derived from the corresponding anomalous fields. These quantities are area-averaged separately over the UB region and the Eurasian continent. It can be found that there is no obvious difference between the low-frequency energy and the difference energy. The low-frequency energy accounts for approximately 100% of the difference energy, which is especially true for $KE_{low}$ and $KE_{total\text{-}high}$. Therefore, the energetics of UBHs has been depicted, at least qualitatively, through the terms in Eqs.

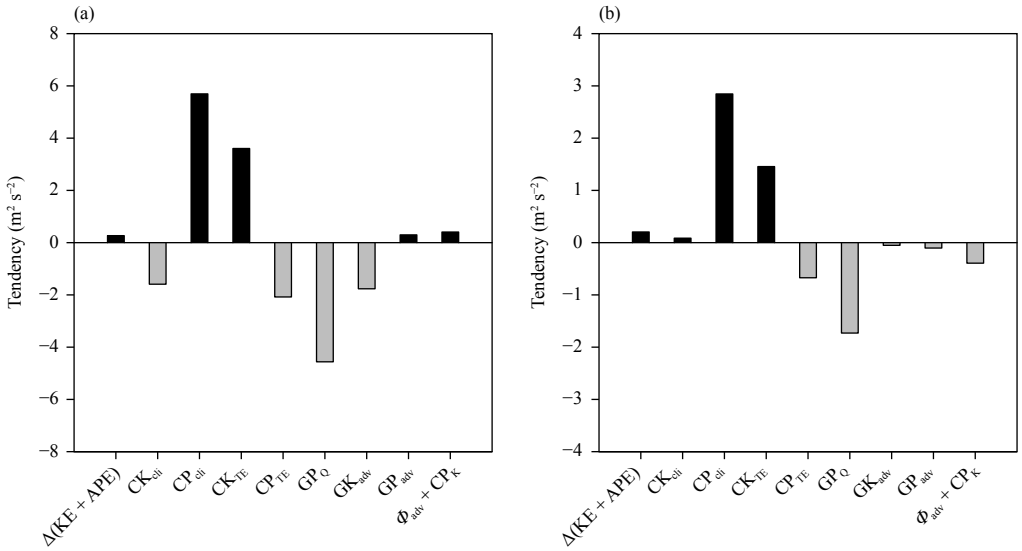


**Fig. 11.** Tendency ($m^2\ s^{-2}$) of total energy (ΔKE + ΔAPE) and each term in Eqs. (2) and (3) for the composite blocking highs over the North Atlantic. All terms are averaged temporally from day −6 to day 6 and spatially from surface ground to 100 hPa and area-weighted averaged over (a) the region with the amplitude of the height anomalies larger than +40 gpm, and (b) the North Atlantic (20°–90°N, 80°W–40°E).

**Table 1.** Low-frequency KE and APE ($m^2 s^{-2}$) for the UBHs from day −4 to day 4

| | UB region (height anomalies greater than +40 gpm) | | Eurasian continent (20°–90°N, 0°–120°E) | |
|---|---|---|---|---|
| Day | $KE_{total\text{-}high}$ (% for $KE_{low}$) | $APE_{total\text{-}high}$ (% for $APE_{low}$) | $KE_{total\text{-}high}$ (% for $KE_{low}$) | $APE_{total\text{-}high}$ (% for $APE_{low}$) |
| −4 | 13.81 (108.48%) | 9.99 (107.52%) | 7.83 (104.94%) | 4.84 (108.14%) |
| −3 | 28.75 (98.18%) | 20.07 (92.02%) | 12.10 (100.3%) | 8.13 (96.22%) |
| −2 | 48.72 (92.81%) | 32.47 (87%) | 17.75 (92.73%) | 12.42 (88.17%) |
| −1 | 62.90 (93.64%) | 39.35 (90.94%) | 21.05 (93.26%) | 15.07 (90.26%) |
| 0 | 59.71 (101.73%) | 35.71 (102.52%) | 20.15 (101.48%) | 14.63 (101.87%) |
| 1 | 50.08 (103.8%) | 29.01 (109.23%) | 17.75 (104.63%) | 13.51 (106.98%) |
| 2 | 38.68 (95.55%) | 21.62 (108.78%) | 14.88 (99.06%) | 11.72 (106.44%) |
| 3 | 21.29 (103.86%) | 15.47 (100.68%) | 10.38 (98.52%) | 9.79 (98.32%) |
| 4 | 10.43 (111.32%) | 10.82 (90.9%) | 6.28 (106.44%) | 7.50 (93.98%) |

Note: The subscript "low" means the energy is derived directly from the low-frequency circulation anomalies, while subscript "total-high" means the energy is derived from subtracting the energy of the high-frequency circulation anomalies from the energy of total circulation anomalies. All results are obtained by integrating from ground to 100 hPa and area-weighted averaged over (1) the UB region where the height anomalies are greater than +40 gpm and (2) the Eurasian continent (20°–90°N, 0°–120°E). The numbers in the brackets indicate the percentage of the energy obtained directly from low-frequency circulation anomalies to the one obtained by subtracting the high-frequency energy from the total energy.

(2) and (3) that are spatially averaged over a certain region in this paper.

Under the background of global warming, there has been an increasing trend in the UBHs frequency since the 1990s (Barnes et al., 2014; Wang and Chen, 2014; Luo et al., 2016a), which is associated with the loss of sea ice over Barents and Kara seas (Honda et al., 2009; Liu et al., 2012; Mori et al., 2014, 2019). Some recent studies further explained that the sea ice loss can lead to the reduction of both the amplitude and vertical shear for the westerlies (Luo et al., 2016a, 2017; Yao et al., 2017) and the meridional gradient of potential vorticity (Luo et al., 2018) over the Eurasian continent, which is favorable for the longer persistence of UBHs. In addition to the above-mentioned variations in the long-term mean basic flow, has the shape of UBHs changed accordingly since the 1990s? From the angle of energetics, either of the changes in the basic flow or the shape of UBHs can contribute to the variation in the conversions of $CP_{cli}$ and/or $CK_{cli}$ (Cai et al., 2007), which is also emphasized by our study on the maintenance of UBHs. It is of interest to quantify the relative changes of $CP_{cli}$ and/or $CK_{cli}$ during the recent decades with respect to the period before the 1990s. It can deepen our understanding on the variations in the dynamics of the UBHs under the background of global warming, which deserves future studies.

***Acknowledgments.*** The authors express sincere thanks to the three anonymous reviewers for their sound criticism and constructive comments that have led to substantial improvement of this paper. The NCAR Command Language (NCL) was used for the calculation and drawing the plots.

## REFERENCES

Barnes, E. A., E. Dunn-Sigouin, G. Masato, et al., 2014: Exploring recent trends in Northern Hemisphere blocking. *Geophys. Res. Lett.*, **41**, 638–644, doi: 10.1002/2013GL058745.

Barriopedro, D., R. García-Herrera, A. R. Lupo, et al., 2006: A climatology of Northern Hemisphere blocking. *J. Climate*, **19**, 1042–1063, doi: 10.1175/JCLI3678.1.

Barriopedro, D., R. García-Herrera, and R. M. Trigo, 2010: Application of blocking diagnosis methods to General Circulation Models. Part I: a novel detection scheme. *Climate Dyn.*, **35**, 1373–1391, doi: 10.1007/s00382-010-0767-5.

Bueh, C., X.-Y. Fu, and Z.-W. Xie, 2011a: Large-scale circulation features typical of wintertime extensive and persistent low temperature events in China. *Atmos. Oceanic Sci. Lett.*, **4**, 235–241, doi: 10.1080/16742834.2011.11446935.

Bueh, C., N. Shi, and Z. W. Xie, 2011b: Large-scale circulation anomalies associated with persistent low temperature over Southern China in January 2008. *Atmos. Sci. Lett.*, **12**, 273–280, doi: 10.1002/asl.333.

Cai, M., and M. Mak, 1990: Symbiotic relation between planetary and synoptic-scale waves. *J. Atmos. Sci.*, **47**, 2953–2968, doi: 10.1175/1520-0469(1990)047<2953:SRBPAS>2.0.CO;2.

Cai, M., S. Yang, H. M. Van Den Dool, et al., 2007: Dynamical implications of the orientation of atmospheric eddies: a local energetics perspective. *Tellus A*, **59**, 127–140, doi: 10.1111/j.1600-0870.2006.00213.x.

Cheung, H. N., W. Zhou, Y. P. Shao, et al., 2013: Observational climatology and characteristics of wintertime atmospheric blocking over Ural–Siberia. *Climate Dyn.*, **41**, 63–79, doi: 10.1007/s00382-012-1587-6.

Colucci, S. J., 1985: Explosive cyclogenesis and large-scale circulation changes: Implications for atmospheric blocking. *J. Atmos. Sci.*, **42**, 2701–2717, doi: 10.1175/1520-0469(1985)042<2701:ECALSC>2.0.CO;2.

Dai, X. L., Y. Zhang, and X.-Q. Yang, 2021: The budget of local available potential energy of low-frequency eddies in Northern Hemispheric winter. *J. Climate*, **34**, 1241–1258, doi: 10.1175/JCLI-D-19-1007.1.

Deng, Y., and M. Mak, 2005: An idealized model study relevant to the dynamics of the midwinter minimum of the Pacific storm track. *J. Atmos. Sci.*, **62**, 1209–1225, doi: 10.1175/JAS3400.1.

Dole, R. M., and N. D. Gordon, 1983: Persistent anomalies of the extratropical Northern Hemisphere wintertime circulation: Geographical distribution and regional persistence characteristics. *Mon. Wea. Rev.*, **111**, 1567–1586, doi: 10.1175/1520-0493(1983)111<1567:PAOTEN>2.0.CO;2.

Duchon, C. E., 1979: Lanczos filtering in one and two dimensions. *J. Appl. Meteor.*, **18**, 1016–1022, doi: 10.1175/1520-0450(1979)018<1016:LFIOAT>2.0.CO;2.

Green, J. S. A., 1977: The weather during July 1976: Some dynamical considerations of the drought. *Weather*, **32**, 120–126, doi: 10.1002/j.1477-8696.1977.tb04532.x.

Hansen, A. R., and T.-C. Chen, 1982: A spectral energetics analysis of atmospheric blocking. *Mon. Wea. Rev.*, **110**, 1146–1165, doi:10.1175/1520-0493(1982)110<1146:ASEAOA>2.0.CO;2.

Hansen, A. R., and A. Sutera, 1984: A comparison of the spectral energy and enstrophy budgets of blocking versus nonblocking periods. *Tellus A*, **36**, 52–63, doi: 10.3402/tellusa.v36i1.11465.

Holopainen, E., and C. Fortelius, 1987: High-frequency transient eddies and blocking. *J. Atmos. Sci.*, **44**, 1632–1645, doi: 10.1175/1520-0469(1987)044<1632:HFTEAB>2.0.CO;2.

Honda, M., J. Inoue, and S. Yamane, 2009: Influence of low Arctic sea-ice minima on anomalously cold Eurasian winters. *Geophys. Res. Lett.*, **36**, L08707, doi: 10.1029/2008GL037079.

Hoskins, B. J., I. N. James, and G. H. White, 1983: The shape, propagation and mean-flow interaction of large-scale weather systems. *J. Atmos. Sci.*, **40**, 1595–1612, doi: 10.1175/1520-0469(1983)040<1595:TSPAMF>2.0.CO;2.

Huang, C. S. Y., and N. Nakamura, 2016: Local finite-amplitude wave activity as a diagnostic of anomalous weather events. *J. Atmos. Sci.*, **73**, 211–229, doi: 10.1175/JAS-D-15-0194.1.

Illari, L., and J. C. Marshall, 1983: On the interpretation of eddy fluxes during a blocking episode. *J. Atmos. Sci.*, **40**, 2232–2242, doi: 10.1175/1520-0469(1983)040<2232:OTIOEF>2.0.CO;2.

Jiang, T. Y., Y. Deng, and W. H. Li, 2013: Local kinetic energy budget of high-frequency and intermediate-frequency eddies: winter climatology and interannual variability. *Climate Dyn.*, **41**, 961–976, doi: 10.1007/s00382-013-1684-1.

Joung, C. H., and M. H. Hitchman, 1982: On the role of successive downstream development in East Asian polar air outbreaks. *Mon. Wea. Rev.*, **110**, 1224–1237, doi: 10.1175/1520-0493(1982)110<1224:OTROSD>2.0.CO;2.

Kobayashi, S., Y. Ota, Y. Harada, et al., 2015: The JRA-55 reanalysis: General specifications and basic characteristics. *J. Meteor. Soc. Japan*, **93**, 5–48, doi: 10.2151/jmsj.2015-001.

Kosaka, Y., and H. Nakamura, 2006: Structure and dynamics of the summertime Pacific–Japan teleconnection pattern. *Quart. J. Roy. Meteor. Soc.*, **132**, 2009–2030, doi: 10.1256/qj.05.204.

Kosaka, Y., and H. Nakamura, 2010: Mechanisms of meridional teleconnection observed between a summer monsoon system and a subtropical anticyclone. Part I: The Pacific–Japan pattern. *J. Climate*, **23**, 5085–5108, doi: 10.1175/2010JCLI3413.1.

Kosaka, Y., H. Nakamura, M. Watanabe, et al., 2009: Analysis on the dynamics of a wave-like teleconnection pattern along the summertime Asian jet based on a reanalysis dataset and climate model simulations. *J. Meteor. Soc. Japan*, **87**, 561–580, doi: 10.2151/jmsj.87.561.

Lau, N.-C., and E. O. Holopainen, 1984: Transient eddy forcing of the time-mean flow as identified by geopotential tendencies. *J. Atmos. Sci.*, **41**, 313–328, doi: 10.1175/1520-0469(1984)041<0313:TEFOTT>2.0.CO;2.

Li, S. L., 2004: Impact of northwest Atlantic SST anomalies on the circulation over the Ural Mountains during early winter. *J. Meteor. Soc. Japan*, **82**, 971–988, doi: 10.2151/jmsj.2004.971.

Li, Y., Y. Lu, and C. H. Wang, 2020: Characteristics of thermal and momentum transport during the lifetime of Ural blocking highs. *Int. J. Climatol.*, **40**, 77–93, doi: 10.1002/joc.6195.

Liang, X. S., 2016: Canonical transfer and multiscale energetics for primitive and quasigeostrophic atmospheres. *J. Atmos. Sci.*, **73**, 4439–4468, doi: 10.1175/JAS-D-16-0131.1.

Liu, J. P., J. A. Curry, H. J. Wang, et al., 2012: Impact of declining Arctic sea ice on winter snowfall. *Proc. Natl. Acad. Sci. USA*, **109**, 4074–4079, doi: 10.1073/pnas.1114910109.

Lorenz, E. N., 1955: Available potential energy and the maintenance of the general circulation. *Tellus*, **7**, 157–167, doi: 10.3402/tellusa.v7i2.8796.

Lu, R. Y., and R. H. Huang, 1996: Energetics examination of the blocking episodes in the Northern Hemisphere. *Chinese J. Atmos. Sci.*, **20**, 269–278, doi: 10.3878/j.issn.1006-9895.1996.03.02. (in Chinese)

Luo, D. H., 2000: Planetary-scale baroclinic envelope Rossby solitons in a two-layer model and their interaction with synoptic-scale eddies. *Dyn. Atmos. Oceans*, **32**, 27–74, doi: 10.1016/S0377-0265(99)00018-4.

Luo, D. H., 2005: A barotropic envelope Rossby soliton model for block–eddy interaction. Part I: Effect of topography. *J. Atmos. Sci.*, **62**, 5–21, doi: 10.1175/1186.1.

Luo, D. H., A. R. Lupo, and H. Wan, 2007: Dynamics of eddy-driven low-frequency dipole modes. Part I: A simple model of North Atlantic Oscillations. *J. Atmos. Sci.*, **64**, 3–28, doi: 10.1175/JAS3818.1.

Luo, D. H., J. Cha, L. H. Zhong, et al., 2014: A nonlinear multiscale interaction model for atmospheric blocking: The eddy-blocking matching mechanism. *Quart. J. Roy. Meteor. Soc.*, **140**, 1785–1808, doi: 10.1002/qj.2337.

Luo, D. H., Y. Yao, and A. G. Dai, 2015: Decadal relationship between European blocking and the North Atlantic Oscillation during 1978–2011. Part II: A theoretical model study. *J. Atmos. Sci.*, **72**, 1174–1199, doi: 10.1175/JAS-D-14-0040.1.

Luo, D. H., Y. Q. Xiao, Y. Yao, et al., 2016a: Impact of Ural blocking on winter warm Arctic–cold Eurasian anomalies. Part I: Blocking-induced amplification. *J. Climate*, **29**, 3925–3947, doi: 10.1175/JCLI-D-15-0611.1.

Luo, D. H., Y. Q. Xiao, Y. N. Diao, et al., 2016b: Impact of Ural blocking on winter warm Arctic–cold Eurasian anomalies. Part II: The link to the North Atlantic Oscillation. *J. Climate*, **29**, 3949–3971, doi: 10.1175/JCLI-D-15-0612.1.

Luo, D. H., Y. Yao, A. G. Dai, et al., 2017: Increased quasi stationarity and persistence of winter Ural blocking and Eurasian extreme cold events in response to Arctic warming. Part II: A theoretical explanation. *J. Climate*, **30**, 3569–3587, doi: 10.1175/JCLI-D-16-0262.1.

Luo, D. H., X. D. Chen, A. G. Dai, et al., 2018: Changes in atmospheric blocking circulations linked with winter Arctic warming: A new perspective. *J. Climate*, **31**, 7661–7678, doi: 10.1175/JCLI-D-18-0040.1.

Luo, D. H., W. Q. Zhang, L. H. Zhong, et al., 2019: A nonlinear theory of atmospheric blocking: A potential vorticity gradient view. *J. Atmos. Sci.*, **76**, 2399–2427, doi: 10.1175/JAS-D-18-0324.1.

Lupo, A. R., and P. J. Smith, 1995: Climatological features of

blocking anticyclones in the Northern Hemisphere. *Tellus A*, **47**, 439–456, doi: 10.3402/tellusa.v47i4.11527.

Ma, J. W., and X. S. Liang, 2017: Multiscale dynamical processes underlying the wintertime Atlantic blockings. *J. Atmos. Sci.*, **74**, 3815–3831, doi: 10.1175/JAS-D-16-0295.1.

Mak, M., and M. Cai, 1989: Local barotropic instability. *J. Atmos. Sci.*, **46**, 3289–3311, doi: 10.1175/1520-0469(1989)046<3289:LBI>2.0.CO;2.

Matsueda, M., and T. N. Palmer, 2018: Estimates of flow-dependent predictability of wintertime Euro-Atlantic weather regimes in medium-range forecasts. *Quart. J. Roy. Meteor. Soc.*, **144**, 1012–1027, doi: 10.1002/qj.3265.

Mori, M., M. Watanabe, H. Shiogama, et al., 2014: Robust Arctic sea-ice influence on the frequent Eurasian cold winters in past decades. *Nat. Geosci.*, **7**, 869–873, doi: 10.1038/ngeo2277.

Mori, M., Y. Kosaka, M. Watanabe, et al., 2019: A reconciled estimate of the influence of Arctic sea-ice loss on recent Eurasian cooling. *Nat. Climate Change*, **9**, 123–129, doi: 10.1038/s41558-018-0379-3.

Mullen, S. L., 1987: Transient eddy forcing of blocking flows. *J. Atmos. Sci.*, **44**, 3–22, doi: 10.1175/1520-0469(1987)044<0003:TEFOBF>2.0.CO;2.

Nakamura, H., 1994: Rotational evolution of potential vorticity associated with a strong blocking flow configuration over Europe. *Geophys. Res. Lett.*, **21**, 2003–2006, doi: 10.1029/94GL01614.

Nakamura, H., and T. Fukamachi, 2004: Evolution and dynamics of summertime blocking over the Far East and the associated surface Okhotsk high. *Quart. J. Roy. Meteor. Soc.*, **130**, 1213–1233, doi: 10.1256/qj.03.101.

Nakamura, H., M. Tanaka, and J. M. Wallace, 1987: Horizontal structure and energetics of Northern Hemisphere wintertime teleconnection patterns. *J. Atmos. Sci.*, **44**, 3377–3391, doi: 10.1175/1520-0469(1987)044<3377:HSAEON>2.0.CO;2.

Nakamura, H., M. Nakamura, and J. L. Anderson, 1997: The role of high- and low-frequency dynamics in blocking formation. *Mon. Wea. Rev.*, **125**, 2074–2093, doi: 10.1175/1520-0493(1997)125<2074:TROHAL>2.0.CO;2.

Nakamura, N., and C. S. Y. Huang, 2018: Atmospheric blocking as a traffic jam in the jet stream. *Science*, **361**, 42–47, doi: 10.1126/science.aat0721.

Overland, J. E., and M. Y. Wang, 2010: Large-scale atmospheric circulation changes are associated with the recent loss of Arctic sea ice. *Tellus A*, **62**, 1–9, doi: 10.1111/j.1600-0870.2009.00421.x.

Pelly, J. L., and B. J. Hoskins, 2003: A new perspective on blocking. *J. Atmos. Sci.*, **60**, 743–755, doi: 10.1175/1520-0469(2003)060<0743:ANPOB>2.0.CO;2.

Pfahl, S., C. Schwierz, M. Croci-Maspoli, et al., 2015: Importance of latent heat release in ascending air streams for atmospheric blocking. *Nat. Geosci.*, **8**, 610–614, doi: 10.1038/ngeo2487.

Schwierz, C., M. Croci-Maspoli, and H. C. Davies, 2004: Perspicacious indicators of atmospheric blocking. *Geophys. Res. Lett.*, **31**, L06125, doi: 10.1029/2003GL019341.

Shi, N., X. Q. Wang, L. Y. Zhang, et al., 2016: Features of Rossby wave propagation associated with the evolution of summertime blocking highs with different configurations over northeast Asia. *Mon. Wea. Rev.*, **144**, 2531–2546, doi: 10.1175/MWR-D-15-0369.1.

Shi, N., SuolangTajie, P. Y. Tian, et al., 2020: Contrasting relationship between wintertime blocking highs over Europe–Siberia and temperature anomalies in the Yangtze River basin. *Mon. Wea. Rev.*, **148**, 2953–2970, doi: 10.1175/MWR-D-19-0152.1.

Shutts, G. J., 1983: The propagation of eddies in diffluent jetstreams: Eddy vorticity forcing of 'blocking' flow fields. *Quart. J. Roy. Meteor. Soc.*, **109**, 737–761, doi: 10.1002/qj.49710946204.

Simmons, A. J., J. M. Wallace, and G. W. Branstator, 1983: Barotropic wave propagation and instability, and atmospheric teleconnection patterns. *J. Atmos. Sci.*, **40**, 1363–1392, doi: 10.1175/1520-0469(1983)040<1363:BWPAIA>2.0.CO;2.

Takaya, K., and H. Nakamura, 2001: A formulation of a phase-independent wave-activity flux for stationary and migratory quasigeostrophic eddies on a zonally varying basic flow. *J. Atmos. Sci.*, **58**, 608–627, doi: 10.1175/1520-0469(2001)058<0608:AFOAPI>2.0.CO;2.

Takaya, K., and H. Nakamura, 2005: Mechanisms of intraseasonal amplification of the cold Siberian high. *J. Atmos. Sci.*, **62**, 4423–4440, doi: 10.1175/JAS3629.1.

Tanaka, S., K. Nishii, and H. Nakamura, 2016: Vertical structure and energetics of the western Pacific teleconnection pattern. *J. Climate*, **29**, 6597–6616, doi: 10.1175/JCLI-D-15-0549.1.

Tao, S. Y., 1957: *A Study of Activities of Cold Airs in East Asian Winter*, *Handbook of Short-Term Forecast*. Meteorology Press, Beijing, 60–92. (in Chinese)

Tibaldi, S., and F. Molteni, 1990: On the operational predictability of blocking. *Tellus A*, **42**, 343–365, doi: 10.3402/tellusa.v42i3.11882.

Trenberth, K. E., 1986: An assessment of the impact of transient eddies on the zonal flow during a blocking episode using localized Eliassen–Palm flux diagnostics. *J. Atmos. Sci.*, **43**, 2070–2087, doi: 10.1175/1520-0469(1986)043<2070:AAOTIO>2.0.CO;2.

Wang, L., and W. Chen, 2014: The East Asian winter monsoon: re-amplification in the mid-2000s. *Chinese Sci. Bull.*, **59**, 430–436, doi: 10.1007/s11434-013-0029-0.

Wang, M. L., Y. Zhang, and J. Lu, 2021: The evolution dynamical processes of Ural blocking through the lens of local finite-amplitude wave activity budget analysis. *Geophys. Res. Lett.*, **48**, e2020GL091727, doi: 10.1029/2020GL091727.

Wen, M., S. Yang, A. Kumar, et al., 2009: An analysis of the large-scale climate anomalies associated with the snowstorms affecting China in January 2008. *Mon. Wea. Rev.*, **137**, 1111–1131, doi: 10.1175/2008MWR2638.1.

Wilks, D. S., 2016: "The stippling shows statistically significant grid points": How research results are routinely overstated and overinterpreted, and what to do about it. *Bull. Amer. Meteor. Soc.*, **97**, 2263–2273, doi: 10.1175/BAMS-D-15-00267.1.

Woollings, T., D. Barriopedro, J. Methven, et al., 2018: Blocking and its response to climate change. *Curr. Clim. Change Rep.*, **4**, 287–300, doi: 10.1007/s40641-018-0108-z.

Yao, Y., D. H. Luo, A. G. Dai, et al., 2017: Increased quasi stationarity and persistence of winter Ural blocking and Eurasian extreme cold events in response to Arctic warming. Part I: Insights from observational analyses. *J. Climate*, **30**, 3549–3568, doi: 10.1175/JCLI-D-16-0261.1.

Zhou, W., J. C. L. Chan, W. Chen, et al., 2009: Synoptic-scale

controls of persistent low temperature and icy weather over southern China in January 2008. *Mon. Wea. Rev.*, **137**, 3978–3991, doi: 10.1175/2009MWR2952.1.

Zhuge, A. R., and B. K. Tan, 2021a: The springtime western Pacific pattern: Its formation and maintenance mechanisms and climate impacts. *J. Climate*, **34**, 4913–4936, doi: 10.1175/JCLI-D-20-0051.1.

Zhuge, A. R., and B. K. Tan, 2021b: The zonal North Pacific Oscillation: a high-impact atmospheric teleconnection pattern influencing the North Pacific and North America. *Environ. Res. Lett.*, **16**, 074007, doi: 10.1088/1748-9326/ac037b.

Tech & Copy Editor: Qi WANG